From *in silico* prediction to experimental validation: Identification of drugs and novel synergistic combinations that inhibit growth of inflammatory breast cancer cells

Esraa A. Salim[1], Xiaojia Ji[1], Michael Tarpley[1], Maria S. Dixon[1], Weifan Zheng[1,2], John E. Scott[1,2*], Kevin P. Williams[1,2*]

[1] Biomanufacturing Research Institute and Technology Enterprise, North Carolina Central University, Durham, NC, USA

[2] Department of Pharmaceutical Sciences, North Carolina Central University, Durham, NC, USA

* Corresponding authors:

Email: kpwilliams@nccu.edu (K.P.W.); jscott@nccu.edu (J.E.S.)

Abstract

Drug repurposing offers a promising approach for identifying novel treatments, especially for rare cancers like inflammatory breast cancer (IBC), an aggressive type with limited therapeutic options. Here, we present a comprehensive validation and verification study of compounds identified through two computational approaches: Literature Wide Association Studies (LWAS) and Gene Reversal Rate (GRR), using orthogonal cell viability assays in 2D models across IBC and non-IBC cell lines. In the SUM149 IBC cell line, repurposed compounds predicted from LWAS achieved a 70% success rate, with several showing nanomolar potency, while those predicted from GRR showed a 38% success rate. Through systematic combination screening in both 2D and 3D-spheroid models, we identified novel synergistic compound pairs targeting crosstalk between IGF1-R, EGFR and PI3K/Akt/mTOR pathways, with high synergy scores across multiple reference models. Using these combinations, western blotting analysis revealed significant suppression in the phosphorylation of key signaling proteins and downstream effectors, while wound healing assays demonstrated reduced cell migration for some combinations, suggesting effective pathway inhibition. To further validate these findings at the transcriptional level, RNA-Seq analysis in SUM149 cells confirmed that the GRR drug combinations significantly reversed the IBC gene expression signature (IBC-GES). These findings not only validated our computational predictions but also identified promising combination strategies that could potentially overcome drug resistance in IBC. Our integrated computational-experimental approach establishes a framework for systematic drug repurposing and highlights novel therapeutic combinations warranting further investigation.

Keywords inflammatory breast cancer (IBC); breast cancer; drug repurposing; drug combinations; PI3K/Akt/mTOR; SUM149, RNA-Seq.

Introduction

Inflammatory breast cancer (IBC) is an aggressive and uncommon type of breast cancer [1-3]. In Western nations, IBC accounts for up to 5% of breast cancer cases [4, 5], with higher rates among African American [6] and North African populations, reaching 7-11.1% [7]. Although considered rare, IBC is responsible for 8-10% of all breast cancer deaths [8]. At diagnosis, up to 85% of IBC patients have lymph node involvement, and up to 30% show distant metastasis [9, 10]. The aggressive nature of IBC and the presence of unique characteristics in its presentation [11, 12] and progression contribute significantly to the higher rates of treatment resistance, relapse, and mortality [13]. Despite the widespread adoption of trimodality treatment for IBC, combining anthracycline- and taxane-based neoadjuvant chemotherapy (NACT), surgery, and radiation therapy [14], the 5-year and 10-year overall survival (OS) rates remain low at 55.4% and 37.3%, respectively [15, 16]. Currently, there is no Food and Drug Administration (FDA)-approved targeted therapy specific to IBC and the current treatment strategies are primarily based on findings from studies of high-risk non-IBC patients [17]. This critical gap in treatment options highlights the essential need for innovative therapeutic strategies to improve patient outcomes in rare diseases. Several drug discovery approaches can be undertaken to find novel drugs for IBC, including drug repurposing which can be a promising approach to address this critical need for new treatments.

Drug repurposing, the application of existing, market-approved drugs to new disease indications, offers significant advantages over *de novo* drug discovery [18]. This approach aims to enhance the drug discovery process, by reducing both time and cost [19, 20]. By utilizing known drugs with established safety profiles, drug repurposing can bypass intermediate steps

62 and accelerate the path from hypothesis to clinical application [21-23]. The primary objective
63 of drug repurposing is to identify novel associations between existing drugs and diseases
64 through two main approaches: computational prediction and experimental validation [24].
65 Modern computational drug repurposing technologies seek to systemically analyze diverse
66 data types, including genomic, proteomic, clinical health records, and scientific literature to
67 predict potential drug-disease connections [20, 25, 26]. Our previous studies utilized two
68 distinct computational approaches [27, 28] to identify repurposing candidates for IBC
69 treatment. Our first approach utilized Literature Wide Association Study (LWAS) [27], which
70 applies extensive text mining [29] as a powerful tool to identify new repurposed candidates.
71 Our second approach used Gene Reversal Rate (GRR) [28], which employs gene expression
72 reversal methodology [30, 31] to identify compounds that are capable of reversing cancer-
73 associated gene expression patterns. Complementing these computational methods,
74 experimental validation approaches involve direct testing of the predicted compounds in
75 various disease models to enhance the likelihood of successful drug repurposing.

76 This current study aimed to assess the efficacy of the drug and compound candidates
77 we had predicted for IBC from our LWAS and GRR approaches using *in vitro* screening
78 techniques in 2D and 3D IBC and non-IBC cell-based models. We used different cell viability
79 and proliferation assays to evaluate drug potency and efficacy, both as single agents and in
80 combinations. Our initial findings identified anti-proliferative effects for a subset of drugs in
81 both IBC and non-IBC cell lines, with 70% (19 of 24) of the LWAS-predicted compounds and
82 38% (6 of 16) of the GRR-predicted compounds showing efficacy in the SUM149 IBC cell
83 line. To address potential drug resistance to single compounds, we used a drug combination
84 assay matrix and synergy analysis pipeline to identify potential synergistic combinations. Three
85 novel synergistic combinations were identified with significant effects on proliferation,
86 spheroid integrity, protein expression, and cell migration in IBC cell models. These

87 combinations comprising compounds predicted from our GRR study and had not been
88 previously reported in IBC clinical trials or the literature. In addition to the phenotypic and
89 protein-level validation, we further assessed transcriptional responses to these GRR drug
90 combinations using RNA-Seq and observed a significant reversal of genes in the IBC gene
91 expression signature. In this study, the synergistic GRR combinations that we identified act on
92 insulin-like growth factor 1 receptor (IGF1-R) and epidermal growth factor receptor (EGFR)
93 signaling, as well as downstream PI3K/Akt/mTOR signaling, suggesting a promising avenue
94 for targeting IBC.

95 Materials and methods

96 Cell lines and compounds

97 Four breast cancer cell lines were used in this study: SUM149PT (SUM149) and
98 SUM159PT (SUM159) (obtained from BioIVT, Westbury, NY, USA), and MDA-MB-231 and
99 MCF-7 (obtained from American Type Culture Collection, ATCC, Manassas, VA, USA).
100 Compounds identified through LWAS [27] (n = 24) and GRR [28] (n = 16 were commercially
101 available out of the 19 identified) studies were purchased from Selleck Chemicals (Houston,
102 TX, USA) and Sigma-Aldrich (St. Louis, MO, USA). All compounds were supplied as
103 powders, reconstituted in 100% DMSO to a stock concentration of 10 mM, and stored at -20°C.

104 Cell culture

105 SUM149 and SUM159 cells were cultured in Ham's F-12 medium supplemented with
106 5% FBS, 1 µg/ml hydrocortisone, 5 µg/ml insulin, 1% of 10,000 units/mL
107 Penicillin/Streptomycin, and 10 mM HEPES, according to BioIVT guidelines. MCF-7 cells
108 were maintained in EMEM supplemented with 0.01 mg/ml human recombinant insulin, 10%
109 FBS, and 1% Penicillin/Streptomycin, following ATCC protocols. MDA-MB-231 cells were

110 cultured in Leibovitz's L-15 Medium supplemented with 10% FBS and 1%
111 Penicillin/Streptomycin, as recommended by ATCC. SUM149, SUM159, and MCF-7 cells
112 were incubated at 37°C in a humidified atmosphere with 5% CO_2. MDA-MB-231 cells were
113 maintained at 37°C with free gas exchange and 0% CO_2.

114 High content imaging cell proliferation assay

115 Cell proliferation was quantified using an automated Hoechst 33342 DNA staining
116 method, as previously described [32, 33]. Breast cancer cell lines (SUM149, SUM159, MDA-
117 MB-231, and MCF-7) were seeded in 384-well microplates (Corning, 3764) at optimized
118 densities of 800, 600, 1600, and 2500 cells/well, respectively. Cell suspensions were dispensed
119 at 50 µL per well using a MultiFlo Dispenser (Agilent BioTek). Each plate included negative
120 controls (0.1% DMSO) and positive controls (Staurosporine at 10 µM and 1 µM). After 24
121 hours, cells were treated with test compounds dispensed by a D300 Digital Dispenser (HP Inc.,
122 Palo Alto, CA, USA). The compounds were solubilized in DMSO to prepare 10 mM stock
123 solutions and dispensed in a 20-point dose-response range using 1:2 serial dilutions, starting
124 with 10 µM concentration. After 72 h of treatment, cells were stained with Hoechst 33342
125 using a Biomek NX Automated Workstation (Beckman Coulter, Brea, CA, USA). The dye was
126 added at a final concentration of 10 µg/mL, and plates were incubated for 45 min at 37°C. The
127 culture medium and dye were then aspirated, and cells were fixed with 20 µL of 4% formalin
128 for 15 min at room temperature. After removing the fixative, 50 µL of PBS were added to each
129 well. Cell nuclei were imaged and quantified using a CellInsight CX7 High-Content Screening
130 (HCS) Platform (Thermo Fisher Scientific). Five fields per well were captured using a 10×
131 objective. Data were analyzed using GraphPad Prism 9.0 (GraphPad Software, San Diego, CA,
132 USA). All experiments were performed in triplicate technical replicates with three independent
133 experiments, and results are presented as mean ± SD.

Automated cell viability assay

Cell viability was evaluated in four breast cancer cell lines (SUM149, SUM159, MDA-MB-231, and MCF-7) using an automated high-throughput screening approach [34]. The cells were seeded at optimized densities (SUM149: 800 cells/well; SUM159: 600 cells/well; MDA-MB-231: 4000 cells/well; MCF-7: 2500 cells/well) in 384-well flat-bottom polystyrene microplates (Corning, Cat. #3701). Cell suspensions were dispensed using a MultiFlo Dispenser (Agilent BioTek, Santa Clara, CA, USA) in 50 µL of complete growth medium per well. Following 24 h, cells were treated with test compounds in a dose-response format as described above. Each plate contains maximum solvent control wells (0.1 % DMSO) and minimum control wells (no cells, culture media only). Cell viability was quantified 72 h post-treatment using the MTT (3-(4,5-dimethylthiazol-2-yl)-2,5-diphenyltetrazolium bromide) colorimetric assay. MTT solution was delivered to each well at a final concentration of 0.5 mg/mL using a Biomek NX Automated Workstation (Beckman Coulter, Brea, CA, USA). After a 4 h incubation at 37°C to allow formazan crystal formation, the culture medium was aspirated, and the crystals were solubilized in 40 µL DMSO during a 1 h dark incubation at room temperature. Absorbance was measured at 550 nm using a SpectraMax Microplate Reader (Molecular Devices, San Jose, CA, USA). Cell viability percentages were calculated by normalizing sample absorbance values to negative control measurements. Dose-response curves were generated, and the half-maximal inhibitory concentration (IC_{50}) was calculated using GraphPad Prism 9.0 (GraphPad Software, San Diego, CA, USA). All experiments were conducted in biological triplicate, with data presented as mean ± standard deviation (SD).

Drug combination screening

The synergistic effects of drug combinations were evaluated in 2D SUM149 cells using the Hoechst 33342 DNA staining assay. This assay was performed over five days as described

158 in above. The combination effects were assessed in two sequential phases: primary screening
159 followed by secondary validation screening.

160 Primary combination screening: single-dose drug combinations

161 Every two compounds were combined in the same well at their respective EC_{25} values
162 to get a singular dose. The concentration that achieves 25% inhibition (EC_{25}) values for each
163 drug was calculated using the following equation, in which F is the desired response level, and
164 H is the Hill slope:

165 $$\mathbf{EC_F} = \left(\frac{\mathbf{F}}{\mathbf{100-F}}\right)^{\frac{\mathbf{1}}{\mathbf{H}}} \times \mathbf{EC_{50}} \quad (1)$$

166 In total, 78 combinations from the LWAS study and 15 combinations from the GRR
167 study were evaluated. Synergy analysis was performed using the Bliss excess Independence
168 method [35] using the following equation:

169 $$\mathbf{Bliss\ excess} = \mathbf{Viability}\ (\mathbf{Drug_A} + \mathbf{Drug_B}) - (\mathbf{Viability}\ (\mathbf{Drug_A})\ \mathrm{x}\ \mathbf{Viability}\ (\mathbf{Drug_B})) \quad (2)$$

170

171 The Bliss excess score, with negative values indicating synergy, was calculated across
172 quadruplicate technical replicates to assess statistical significance.

173 Secondary drug combination screening: matrix-designed drug treatments

174 An 8x8 dose-response matrix [36, 37] was designed using ½ log serial dilutions for the
175 top five combinations from each list, based on the Bliss synergy scores from the primary
176 screening. This was implemented using the Synergy Wizard feature in the D300 Control
177 Software (HP Inc.). The highest concentration in each matrix was selected based on each drug's
178 IC_{50} value. Staurosporine (10 μM) was used as a positive control and DMSO (0.2%) as a
179 negative control. DMSO tolerance in SUM149 cells was confirmed up to 0.8%. The experiment
180 was conducted with three technical replicates and three independent experiments. Percent

181 inhibition and synergy scores were calculated and analyzed using SynergyFinder3 [38]
182 SynergyFinder+ [39] web-based tools.

183 Quantification of cell viability in SUM149 spheroids

184 Cell viability was assessed using the CellTiter-Glo Luminescent Cell Viability Assay
185 (Promega, Madison, WI, USA) according to the manufacturer's instructions. Briefly, SUM149
186 cells were plated in 384 microplates (Corning, Cat. #3830) at 5000 cells per well and allowed
187 to form a spheroid for 72 h at 37°C in a humidified 5% CO_2 incubator. Spheroids were then
188 treated with selected combinations (based on a 2D combination experiment) in an 8x8 matrix
189 as described previously, using Staurosporine and DMSO as controls. After 72 h, plates were
190 incubated at room temperature for 30 min. An equal volume of CellTiter-Glo reagent was
191 added to each well, and plates were then shaken on a shaker for 5 minutes to promote cell lysis,
192 followed by 30 min incubation at room temperature. Luminescence was measured using a
193 PHERAstar FSX detection system (BMG LABTECH, Cary, NC, USA). Cell viability was
194 calculated as a percentage relative to vehicle-treated control cells. Each experiment was
195 performed in triplicate and repeated in three independent experiments. Data were analyzed
196 using SynergyFinder+ and SynergyFinder 3 web-based tools.

197 Cell death evaluation and spheroid imaging

198 SYTOX Red Dead Cell Stain (Invitrogen, Cat. No. S34859) was used as a qualitative
199 tool to assess and image the spheroid shape and integrity. Spheroids were formed and treated
200 in 384-well microplates as described above in the CellTiter-Glo assay (2.6). SYTOX Red was
201 added to a final concentration of 40 nM immediately after treatment. Imaging was performed
202 using an IncuCyte S3 Live-Cell Analysis System (Sartorius, Ann Arbor, MI, USA) equipped
203 with a 10× objective. The IncuCyte system was maintained at 37°C and 5% CO_2 throughout
204 the experiment. Images were acquired every 6 h for 3 days, capturing both brightfield and red

205 fluorescence (excitation 585 nm, emission 635 nm) channels. Spheroid size and fluorescence
206 intensity were quantified using the IncuCyte S3 software. A minimum of four spheroids were
207 analyzed per condition.

208 Wound healing and cell migration

209 SUM149 cells were seeded at 60,000 cells per well in an interlock 96-well plate (Essen
210 Bioscience, Ann Arbor, Michigan) and allowed to attach overnight at 37°C in a humidified
211 atmosphere with 5% CO_2. A uniform vertical scratch wound was created across all wells using
212 the automated WoundMaker™ tool (Essen BioScience). Cells were gently washed with media
213 to remove detached cells, and fresh culture medium was added before the combination
214 treatment using a D300 Digital Dispenser (HP). Cell migration into the wound area was
215 monitored in real-time using the IncuCyte® S3 Live-Cell Analysis System (Sartorius) as
216 previously described [33]. Images were automatically captured at 0, 6-, 12-, 18-, and 24-h post-
217 wounding using a 10× objective lens, enabling quantitative assessment of wound closure
218 kinetics.

219 Western blotting

220 SUM149 cell lysates (after 24 h drug treatment) were collected using M-PER buffer
221 supplemented with protease/phosphatase inhibitors (Thermo Fisher Scientific, Cat. #A32959).
222 Lysates were centrifuged (14,000 xg, 15 min, 4°C) and protein concentrations were determined
223 by BCA assay (Pierce, Cat. #23225). Equal protein amounts (15-30 µg/lane) were loaded, and
224 samples were electrophoresed on 4-12% Bis-Tris gels (Invitrogen, Cat. #NP0336BOX). For
225 mTOR and p-mTOR, samples were run on 8% Tris-Glycine gels (Invitrogen, Cat.
226 #XP00085BOX). Proteins were transferred to 0.45 µm PVDF membranes (Invitrogen, Cat.
227 #LC2005) using XCell II™ Blot Module (Overnight, 4°C). Membranes were blocked with 5%
228 BSA in TBS (pH 7.4) for 1 h at room temperature. Primary antibodies were diluted in 5% BSA

229 in TBS-T (0.1% Tween-20) and incubated with membranes overnight at 4°C. All primary
230 antibodies were used at 1:1000 dilution except anti-β-Actin and p-Akt(Ser473) which were
231 used at 1:2000. Antibodies included: anti-β-Actin (45 kDa, LI-COR, #926-42212), AKT (60
232 kDa, CST, #9272), p-Akt(Ser473) (60 kDa, CST, #4060), IGF-1R (95 kDa, CST, #3027), p-
233 IGF-1R(Tyr1135/1136) (95 kDa, CST, #3024), EGFR (175 kDa, CST, #4267), p-
234 EGFR(Tyr1068) (175 kDa, CST, #3777), mTOR (289 kDa, CST, #2983), and p-
235 mTOR(Ser2448) (289 kDa, CST, #2971). After TBS-T washes (3×10 min), membranes were
236 incubated with either IRDye secondary antibodies (800CW/680RD, LI-COR, 1:20,000 in 5%
237 BSA/TBS-T [0.2% Tween-20]/0.02% SDS) or HRP-linked antibody (1:10,000, CST, 7074)
238 for 1 h at room temperature. Following TBS-T washes (3×5 min), membranes were imaged
239 using Odyssey CLx (LI-COR) or iBright Systems (Invitrogen). For IGF1-R and pIGF1-R (and
240 β-Actin control for these samples), HRP secondary antibody was used for detection, and blots
241 imaged by iBright. Analysis was performed using Image Studio (v5.2, LI-COR) or iBright
242 software. Band intensities were normalized to total protein stain (for LI-COR) and β-Actin (for
243 iBright). Experiments were performed in triplicate (n=3), with significance determined as $p <$
244 0.05.

245 RNA extraction and RNA Seq analysis

246 Total RNA was extracted from SUM149 cultured cells after 24 h treatment with either
247 combinations or DMSO vehicle control, using the RNeasy Mini Kit (Qiagen, 74104), following
248 the manufacturer's instructions. RNA concentration and purity were assessed using a
249 NanoDrop 2000 spectrophotometer (Thermo Fisher Scientific). The absorbance ratios
250 A260/A280 and A260/A230 were used to evaluate RNA quality and purity. Samples with
251 A260/A280 ratios between 1.8 and 2.1 and A260/A230 ratios above 1.8 were considered of
252 suitable quality for RNA-Seq analysis. All samples were prepared as independent replicates (n
253 = 3). RNA-Seq analysis was performed by Novogen (Novogene Corporation Inc., Sacramento,

254 CA, USA) following their standard pipeline, beginning with the preparation of RNA-Seq
255 libraries using the KAPA mRNA HyperPrep kit, which were then sequenced on an Illumina
256 NovaSeq 6000/X Plus platform to produce 100-bp paired-end reads. Raw reads underwent
257 quality control with FastQC; adapters and low-quality bases were trimmed using fastq-mcf and
258 cutadapt. Potential contaminants (rRNA, tRNA, adapters, mitochondrial sequences) were
259 filtered with Bowtie2, and the remaining reads were aligned to the human Ensembl GRCh38
260 (release 87) reference using STAR in two-pass mode. Gene-level counts were assigned with
261 HTSeq and count matrices were normalized with DESeq2 in R. Differential expression was
262 carried out in DESeq2 using contrasts named Control_vs_Case (direction reported for the case
263 group relative to control) with significance defined as padj < 0.05 and $|\text{Log}_2\text{fold-change}| \geq 2$.

264 Data processing and statistical analysis

265 Statistical analyses and data visualizations were performed using GraphPad Prism 9
266 (GraphPad Software, Inc., San Diego, CA, USA), with statistical significance set at $p < 0.05$
267 for all analyses. IC_{50} values were determined using nonlinear logistic regression analysis with
268 a three-parameter log(inhibitor) vs. dose-response function, constrained to a zero-bottom
269 asymptote. SynergyFinder3 and SynergyFinder+, web-based tools, were used to calculate
270 synergy scores based on four widely used reference models: Bliss, Loewe, Highest Single
271 Agent (HSA), and Zero interaction potency (ZIP). All data are presented as mean ± SD, unless
272 otherwise noted.

Results

Assessment of LWAS and GRR drug candidates for inhibitory effects in breast cancer cell lines

To assess the efficacy of the identified drug and compound candidates from our previous LWAS [27] and GRR [28] studies, we conducted high-throughput screening (HTS) using dose-response treatments in an automated 384-well format. Two orthogonal cell-based assays were utilized to determine the efficacy and potency of each candidate: the Hoechst 33342 assay, a fluorescent DNA staining method for assessing nuclei count (as a readout for cell number) using high-content imaging [32], and the MTT assay to assess effects on cell viability. Screening was conducted across a panel of IBC and non-IBC cell lines: SUM149, SUM159, MDA-MB-231, and MCF-7.

Identification of LWAS candidates with effects on cell proliferation

Our previous LWAS text mining study [27], used a natural language processing-based model trained on a large corpus of cancer-related abstracts to identify diseases that co-occur with IBC, with the concept that drugs for those diseases that cluster with IBC can be potentially repurposed for IBC. This LWAS analysis identified oncology-based compounds that we predicted could be repurposed for IBC [27] and comprised 24 compounds, across various mechanistic classes: tyrosine kinase inhibitors (TKIs), antimetabolites, topoisomerase inhibitors/anthracycline antibiotics, microtubule inhibitors, and alkylating agents (**S1 Table**). In this current study, we first assessed the activity of these 24 compounds [27] in our lab-based Hoechst assay to determine effects on cell number and viability. We found significant antiproliferative activity ($IC_{50} < 10$ μM) for 17 compounds in SUM149, 16 in SUM159, and 15 in both MDA-MB-231 and MCF-7 cell lines (shown in heatmap format in **Fig 1A**).

296 Comparative analysis across cell lines revealed a graded pattern of drug sensitivity, with
297 SUM149 demonstrating the highest responsiveness, particularly to microtubule inhibitors and
298 antimetabolites. Analysis of median IC_{50} values across compound classes showed decreasing
299 sensitivity in the following order: SUM149 > SUM159 > MDA-MB-231 > MCF-7, which may
300 correlate with these cells' relative doubling times. Among the compound classes, microtubule
301 inhibitors demonstrated the highest potency, with docetaxel, paclitaxel, and vincristine
302 showing low nanomolar activity (IC_{50}: 0.2-13 nM) across all cell lines. Topoisomerase
303 inhibitors represented the second-highest set of potent compounds, with doxorubicin and
304 daunorubicin achieving IC_{50} values below 0.2 μM. The tyrosine kinase inhibitors lapatinib and
305 sunitinib showed moderate micromolar potency (IC_{50}: 0.57-7.3 μM and 1.4-5.3 μM,
306 respectively), while gefitinib showed selective activity against SUM149 and SUM159 (0.4-10
307 μM, respectively). Within the antimetabolite class, gemcitabine yielded high potency (IC_{50}:
308 0.001-0.29 μM) and cytarabine yielded moderate potency (IC_{50}: 0.023-0.65 μM). The
309 alkylating agent carboplatin established the lowest potency, with activity only in SUM149
310 (IC_{50} = 6.04 μM). The remaining compounds from the LWAS screen (n = 7) showed minimal
311 antiproliferative effects against SUM149 (IC_{50} > 10 μM). Representative dose-response curves
312 (DRC) for SUM149 are shown in **Fig 1B**, while DRCs for SUM159, MDA-MB-231, and MCF-
313 7 cell lines are in **S1 Fig**. Complete IC_{50} values are summarized in **Table 1**.
314

315 **Fig 1. LWAS drug sensitivity profiles in IBC and non-IBC breast cancer cell line panel**
316 **by Hoechst assay.** (A) Heatmaps representing the percent inhibition response for a 2-fold
317 concentration dose-response starting at 10 μM for SUM149, SUM159, MDA-MB-231, and
318 MCF-7. Drug names are listed on the y-axis. The color scale indicates the level of inhibition,
319 with red representing high inhibition (close to 100%) and green representing low inhibition
320 (close to 0%). (B) Representative dose response curves (DRC) for the LWAS drugs with

321 activity in the SUM149 cell line, showing the percent cell count relative to control against drug
322 concentration (μM). Plots are grouped by drug mechanism: antimetabolites, microtubule
323 inhibitors, topoisomerase inhibitors, and tyrosine kinase inhibitors. Data points and error bars
324 represent the mean ± SD. DRCs for the LWAS drugs in SUM159, MDA-MB-231, and MCF-
325 7 are in **S1 Fig**.

326

327 **Table 1. Efficacy of LWAS-predicted drugs and compounds in four breast cancer cell lines: SUM149,**
328 **SUM159, MDA-MB-231, and MCF-7.**

Drug	**SUM149**	**SUM159**	**MDA-MB-231**	**MCF-7**
	(IC_{50} μM)	**(IC_{50} μM)**	**(IC_{50} μM)**	**(IC_{50} μM)**
Docetaxel	0.0004 ± 0.00006	0.0005 ± 0.00002	0.0012 ± 0.0003	0.00085 ± 0.0001
Paclitaxel	0.002 ± 0.0003	0.002 ± 0.0001	0.0025 ± 0.0007	0.002 ± 0.00035
Vincristine	0.004 ± 0.0001	0.003 ± 0.0002	0.009 ± 0.005	0.003 ± 0.00075
Vinorelbine	0.09 ± 0.02	0.07 ± 0.007	0.25 ± 0.08	0.075 ± 0.008
Lapatinib	0.6 ± 0.5	2.1 ± 0.8	6.5 ± 1.04	4 ± 0.4
Sunitinib	1.4 ± 0.3	0.7 ± 0.1	1.9 ± 0.3	3.9 ± 0.85
Gefitinib	0.4 ± 0.16	0.9 ± 0.033	--	--
Doxorubicin	0.01 ± 0.003	0.01 ± 0.001	0.03 ± 0.009	0.08 ± 0.011
Daunorubicin	0.01 ± 0.003	0.02 ± 0.001	0.02 ± 0.005	0.04 ± 0.003
Mitoxantrone	0.005 ± 0.0003	0.01 ± 0.001	0.003 ± 0.0007	0.02 ± 0.009
Etoposide	0.07 ± 0.016	0.1 ± 0.07	1.1 ± 0.5	1.3 ± 0.4
Topotecan	0.008 ± 0.001	0.012 ± 0.0004	0.03 ± 0.01	0.08 ± 0.06
Gemcitabine	0.001 ± 0.0001	0.004 ± 0.0001	0.005 ± 0.002	0.004 ± 0.001
Cytarabine	0.025 ± 0.005	0.023 ± 0.003	0.2 ± 0.1	0.5 ± 0.2
Carboplatin	4.4 ± 0.5	--	--	--
Methotrexate	0.01 ± 0.008	0.01 ± 0.007	0.9 ± 0.12	0.02 ± 0.004
5-Fluorouracil	4.8 ± 0.6	2.4 ± 1.7	12.4 ± 3.9	3.9 ± 3.3

329 IC_{50} values determined for each drug by the Hoechst assay across the cell lines, with values reported as the mean
330 ± SD from 3 independent experiments.

331

332 Identification of GRR candidates with effects on cell proliferation

333 In our previous GRR analysis, we used a compiled IBC-gene expression signature
334 (IBC-GES) to query the LINCS database for drugs that significantly reversed expression of the
335 majority of IBC-GES genes and identified 19 drugs [28]. Here, we evaluate the anti-
336 proliferative activity of these GRR candidates (16 of the 19 were commercially available),
337 using the Hoechst assay in the same four cell lines described above. The GRR candidates
338 showed differential anti-proliferative activity in each cell line, with significant effects (IC_{50} <
339 10 μM) observed for 6 compounds in SUM149, SUM159 and MDA-MB-231, and 5 in MCF-
340 7 cells (represented as heatmaps in **Fig 2A**). Although the GRR list comprises both oncology
341 and non-oncology compounds from diverse drug classes (**S2 Table**), the active compounds
342 were primarily tyrosine kinase inhibitors, with Akt Inhibitor-IV (AKTIV) being an exception.
343 In SUM149, tipifarnib displayed the highest potency (absolute IC_{50} = 0.075 μM), followed by
344 tyrphostin AG-1478 and AKTIV, which showed comparable potency (absolute IC_{50} ≈ 0.2 μM).
345 Tipifarnib showed a biphasic DRC, and upon calculating the relative IC_{50} in SUM149, it shifted
346 to 7 ± 0.2 nM (10-fold increase in potency). Tyrphostin AG-1478 showed a low efficacy curve
347 (indicating antiproliferative activity), its relative IC_{50} in SUM149 shifted to 0.05 ± 0.01 μM (4-
348 fold increase in potency). Temsirolimus displayed varying potency across the 4 cell lines with
349 an absolute IC_{50} of 4.3 μM in SUM149, compared to much higher potency in SUM159, MDA-
350 MB-231, and MCF-7 cell lines (IC_{50} range: 0.2-0.6 nM). Temsirolimus also showed a biphasic
351 DRC in SUM149 cells, with a relative IC_{50} value of 0.1 nM, which is comparable to other cell
352 lines but with lower efficacy (approximately 60% maximum inhibition). MDA-MB-231
353 showed unique sensitivity to nicardipine (projected IC_{50} = 16.7 μM), while showing reduced

354 sensitivity to the other compounds compared to other cell lines. Tyrphostin AG-1478 showed
355 no inhibitory activity in MCF-7, unlike other cell lines. Representative DRCs for SUM149 are
356 shown in **Fig 2B**, while DRCs for SUM159, MDA-MB-231, and MCF-7 cell lines are in **S2**
357 **Fig**, showing a range of responses. The IC_{50} values for the GRR's compounds are summarized
358 in **Table 2**.
359
360 **Fig 2. GRR drug sensitivity profiles in IBC and non-IBC breast cancer cell line panel by**
361 **Hoechst assay.** (A) Heatmaps representing the percent inhibition response for a 2-fold
362 concentration dose-response starting at 10 μM for SUM149, SUM159, MDA-MB-231, and
363 MCF-7. Drug names are listed on the y-axis. The color scale indicates the level of inhibition,
364 with red representing high inhibition (close to 100%) and green representing low inhibition
365 (close to 0%). (B) Representative dose-response curves for active inhibitors BMS-536924,
366 BMS-754807, Akt Inhibitor IV, temsirolimus, tipifarnib, and tyrphostin AG 1478 in the
367 SUM149 cell line, showing the percent cell count relative to control against drug concentration
368 (μM). Data points and error bars represent the mean ± SD. DRCs for SUM159, MDA-MB-
369 231, and MCF-7 are in **S2 Fig**.
370
371 **Table 2. Efficacy of the GRR-predicted drugs and compounds in four breast cancer cell lines: SUM149,**
372 **SUM159, MDA-MB-231, and MCF-7.**

Drug	**SUM149**	**SUM159**	**MDA-MB-231**	**MCF-7**
	(IC_{50} μM)	**(IC_{50} μM)**	**(IC_{50} μM)**	**(IC_{50} μM)**
BMS-536924	1.9 ± 0.1	0.8 ± 0.3	8.3 ± 3.4	1.4 ± 0.1
BMS-754807	0.5 ± 0.1	0.5 ± 0.04	2.0 ± 0.34	0.4± 0.06
AKTIV	0.2 ± 0.008	0.2 ± 0.02	0.1 ± 0.025	0.2 ± 0.03
Temsirolimus	4.3 ± 0.3	0.00034 ± 0.0004	0.0006 ± 0.0004	0.0002 ± 8.29E-05

Tipifarnib	0.08 ± 0.03	0.0008 ± 0.0002	6.0 ± 1.3	5.8 ± 3
Tyrphostin AG-1478	0.2 ± 0.15	3.5 ± 1.4	9.2 ± 4.2	--
Nicardipine	--	--	16.7 ± 6.1	--

373 IC_{50} values determined for each drug by the Hoechst assay across the cell lines, with values reported as the mean
374 ± SD from 3 independent experiments.
375

376 Identification of LWAS and GRR candidates with efficacy in the MTT cell 377 viability assay

378 We also assessed the LWAS and GRR compounds in an orthogonal cell-based assay
379 (MTT) to assess effects on cell viability. Testing of the compounds in the MTT assay yielded
380 IC_{50} values and DRCs comparable to those of the Hoechst assay for both the LWAS (**S3 Fig**)
381 and the GRR (**S4 Fig**) compounds. All the IC_{50} values for the LWAS drugs and GRR
382 compounds in the MTT assay across the 4 cell lines are summarized in **S3 Table**. For the MTT
383 assay, using an activity threshold of $IC_{50} < 10$ μM, the LWAS list screening yielded 17 active
384 compounds in SUM149, 16 in SUM159, 15 in both MDA-MB-231 and MCF-7, whereas the
385 GRR panel yielded 6 anti-proliferative compounds in SUM149, SUM159 and MDA-MB-231,
386 and 5 in MCF-7. The same compounds were active in both the Hoechst and MTT assays and
387 maintained the same overall rank-order of potency. For LWAS compounds tested in the MTT
388 assay, microtubule inhibitors again were the most potent class with nanomolar potency in both
389 assays across all cell lines, and the median docetaxel IC_{50} shifts by <1.5-fold (e.g. 0.0004 μM
390 in SUM149 by Hoechst versus 0.0003 μM by MTT). Likewise, topoisomerase inhibitors retain
391 mid-nanomolar potency, while antimetabolites gemcitabine and cytarabine showed only ≤ 2-
392 fold differences between assays. For the GRR list, the potencies for each compound in both
393 assay formats were comparable, in the range of 1- to 3-fold difference. In SUM149,
394 temsirolimus showed an IC_{50} value of 4.3 μM in the Hoechst assay and 7.3 μM in MTT assay.

395 For AKTIV, BMS-536924 and BMS-754807, the fold shifts are generally below 3, except for
396 a 7-fold change for BMS-754807 in SUM149 (IC_{50}: 3.6 μM in MTT assay 0.5 μM in Hoechst
397 assay). Tyrphostin AG-1478 shows comparable nanomolar activity in SUM149 and
398 comparable micromolar activity SUM159 cell lines. A couple of results were not consistent
399 between the two assay formats; tipifarnib in SUM159, where the IC_{50} was 0.8 nM by Hoechst
400 compared to 2.1 μM by MTT, and gefitinib, which was ~10-fold less potent in SUM159 by
401 MTT (IC_{50}: 11 μM) than by Hoechst (IC_{50}: 0.9 μM). These differences might reflect the
402 mechanism behind each assay where cytostatic effect manifests faster in the nuclear-count
403 readout than in the metabolic assay. But the overall strong concordance between the two assays
404 was about 85 %: individual IC_{50} pairs differed by less than 2-fold, indicating that the viability
405 (MTT) and nuclear count (Hoechst) endpoints read out very similar anti-proliferative effects
406 for most compounds, with SUM149 being the most responsive cell line in both formats.

407 Assessing drug combinations in SUM149 for synergistic effects

408 The potential synergistic effects of drug combinations were assessed in the SUM149
409 cell line as this was our representative IBC model. The SUM149 cell line was derived from an
410 IBC patient tumor [40], and is a well-established model for IBC [33, 34, 41-43]. Our Hoechst
411 and MTT efficacy profiling of single compounds identified the most potent compounds from
412 both the LWAS and GRR lists for subsequent combination studies. These drug-combination
413 experiments were conducted using a two-tiered approach that included primary and secondary
414 screening. In the primary screening, every two compounds were combined and tested at their
415 respective EC_{25} values. The EC_{25} value was chosen to achieve a modest effect on cell viability,
416 thereby minimizing toxicity and avoiding one drug overwhelming the response. In this case,
417 each drug can affect cellular activity without killing most cells, creating an opportunity to
418 observe an extra effect when the drugs are combined [44]. The 17 active LWAS inhibitors were

419 reduced to 13 by excluding less potent compounds with similar mechanisms of action (MOA),
420 yielding a total of 78 unique two-drug combinations. Likewise, combining the 6 GRR
421 inhibitors gave 15 unique two-drug combinations. The Bliss excess scores [35] were calculated,
422 and a one-sample t-test was used to determine the statistical significance. Combinations that
423 showed statistical significance were subsequently validated in the secondary combination
424 screening phase using 8×8 dose-response matrices in 2D cell models and then confirmed in 3D
425 spheroid models to enable a more comprehensive assessment. Synergy evaluation was
426 performed using SynergyFinder3 [38] and SynergyFinder+ [39] online tools. The complete
427 experimental workflow is summarized in **Fig 3**.
428
429 **Fig 3. Workflow for identification and evaluation of synergistic drug combinations.** The
430 screening process began with 17 LWAS inhibitors refined to 13 LWAS inhibitors after
431 excluding less potent compounds with similar mechanisms of action (MOA) plus 6 GRR
432 inhibitors. Primary drug combination screening was done using drug pairs at their respective
433 EC_{25} values. The identified combinations were selected based on Bliss excess scores and
434 statistical significance (p value < 0.05), which identified 25 LWAS and 9 GRR synergistic
435 combinations to be confirmed in the secondary screening phase, utilizing an 8×8 matrix format.
436 The final analysis included synergy assessment and efficacy evaluation in 2D and 3D cell
437 models.
438

439 Identification of key combinations using single-dose primary screening

440 Our initial primary screening analysis, while using only single EC_{25}-dose combinations,
441 revealed potential drug synergy based on Bliss excess score calculations, in which negative
442 values indicate a synergistic effect when starting with cell viability data [35]. Quantitative

443 analysis of the primary combination screen identified 25 synergistic combinations from the
444 LWAS list (**Fig 4A**, 32.1% success rate, $p < 0.05$) and 9 synergistic combinations from the
445 GRR list (**Fig 4B**, 60% success rate, $p < 0.05$). These synergistic combinations demonstrated
446 robust negative excess Bliss scores ranging from -0.16 to -0.27.
447

448 **Fig 4. Drug combinations identified from primary combination screening based on Bliss**
449 **excess scores in SUM149.** Primary drug combination screening was done using drug pairs at
450 their respective EC_{25} values. Each combination is evaluated based on percentage viability, with
451 negative scores indicating synergism. (A) Twenty-five significantly different combinations
452 were identified from the LWAS study and categorized as reported in the literature for IBC
453 (green bars), tested in clinical trials for IBC (red bars), and novel combinations for IBC (blue
454 bars). (B) Nine significantly different combinations were identified from the GRR list, all of
455 which were novel for IBC. Red asterisks indicate statistically significant deviations centered at
456 zero based on a t-test (*$p < 0.05$; **$p < 0.01$; ***$p < 0.001$). Red oval shapes highlight the
457 selected combinations for further screening in the 8×8 matrix.

458

459 For the LWAS primary combination results, 4 of the 25 combinations (red bar color in
460 **Fig 4**) have been previously documented in IBC-related clinical trials registered on
461 ClinicalTrials.gov, including where carboplatin was combined with either doxorubicin
462 (NCT05415215), docetaxel (NCT00251329 and NCT00118053), lapatinib (NCT01426880),
463 or 5-fluorouracil (NCT01036087). These trials either included IBC patients or specifically
464 focused on IBC populations. Further, the combination of carboplatin with gemcitabine is listed
465 as a treatment option for IBC [45]. For the GRR primary combination screen, combinations
466 targeting PI3K/AKT/mTOR downstream pathways, either directly or indirectly, showed high
467 synergy scores, including BMS-536924 (a dual IGF-1R/IR tyrosine kinase inhibitor) with

468 tyrphostin AG 1478 (a selective EGFR tyrosine kinase inhibitor); and BMS-536924 with
469 AKTIV (an inhibitor of Akt phosphorylation). To our knowledge, the remaining LWAS
470 combinations (bars highlighted in blue) and all the GRR pairs represent potential novel
471 therapeutic strategies for IBC.

472 Drug combinations with the highest negative excess Bliss scores (highlighted by red
473 oval shapes in **Fig 4**, along with two previously reported were selected for secondary
474 combination screening and evaluated using 8×8 dose-response matrices.

475 Determination of synergy score based on dose-response combination matrix

476 For our secondary screening, we conducted an 8×8 dose-response matrix analysis (**Fig**
477 **3**) to validate promising drug combinations identified from the primary single-dose
478 combination screening. This approach again focused on evaluating drug synergy for SUM149
479 cell proliferation. For each drug pair (7 for LWAS and 5 for GRR), we designed dose matrices
480 with IC_{50} concentrations positioned centrally, with concentration ranges above and below IC_{50}
481 at ½-log intervals (**S4 Table**). The experimental protocol involved treating SUM149 cells with
482 drug combinations for 72 h, followed by Hoechst dye-based cell counting. Based on the results
483 from our primary combination screening, we selected the top five combinations from both
484 LWAS and GRR lists. Additionally, we included two other combinations from the LWAS list:
485 one documented in the literature [46] and one found in clinical trials [47] (see **Fig. 4**). We
486 conducted a comprehensive synergy and efficacy analysis to identify the optimal combinations.
487 The synergy score calculation is based on four widely used reference models: Bliss, Loewe,
488 HSA, and ZIP [48]. According to the framework proposed by Malyutina *et al* [49], our
489 combinations were classified as synergistic (scores > 5) or antagonistic (scores < -5) when
490 meeting these thresholds across all models as a strict criterion. For the efficacy metric
491 evaluation, we used the Combination Sensitivity Score (CSS) developed by Malyutina *et al*

492 [49]. CSS quantifies combination efficacy against cell proliferation by calculating the mean
493 area under the dose-response curve when titrating one drug against the IC_{50} concentration of
494 the second drug (CSS_1IC50_2 and CSS_2IC50_1). SynergyFinder+ was used to compute the
495 average CSS values for all combinations. In the LWAS combination analysis, we found that
496 none met the strict criterion for overall synergy or antagonism (all the overall synergy (δ) scores
497 fell between -5 and 5 across all reference models, indicating additive effects) (**S5 Fig**). A closer
498 examination of the contour plots was then undertaken, focusing on the Most Synergistic Area
499 (MSA) [38], which represents a 3×3 dose window in the combination matrix that yields the
500 highest positive deviation from the chosen reference model [38]. This analysis of MSA δ scores
501 gave (δ > 5) for five (Loewe model) and seven (HSA model) of the combinations, respectively
502 (**S5 Fig**, **Table 3**). This approach can highlight the dose ranges where the interaction is most
503 pronounced and help in selecting concentration pairs for follow-up validation. For example,
504 we observed that the lapatinib + doxorubicin combination gave scores of 26.2 for Loewe and
505 7.5 for HSA, whereas lapatinib + carboplatin showed scores of 18.6 in Loewe and 10.1 in HSA.
506 However, for the Bliss and ZIP models, MSA δ scores for all these were < 5, reducing
507 confidence that these combinations might be synergistic.

508 In the GRR combination analysis, the BMS-536924 and tyrphostin AG-1478
509 combination exceeded the 5-score threshold at both the overall (ZIP: 7.9, HSA: 11.8, Bliss:
510 7.6, Loewe: 8.6) and MSA (ZIP: 21.5, HSA: 29.9, Bliss: 20.8, Loewe: 26.1) δ scoring levels,
511 with a 74.4% CSS score for efficacy indicating substantial therapeutic potential through dual
512 pathway inhibition. Three other combinations (BMS-536924 + AKTIV; temsirolimus +
513 AKTIV; and BMS-754807 + tyrphostin AG-1478). showed synergistic effects at the MSA
514 level (exceeding the 5-score threshold), while only one showed (BMS-754807 + AKTIV)
515 additive effects. The contour plots of the 2D drug combination experiments are shown in **Fig**
516 **5**. The corresponding overall synergy (δ) scores and MSA δ scores from SynergyFinder3 for

517 all the GRR combinations are shown in **Table 3**. All the remaining LWAS and GRR
518 combinations not shown had δ <5 for all models at both the overall and MSA level.
519

520 **Fig 5. Contour plots of selected GRR drug combinations.** Synergy scores across Bliss, ZIP,
521 Loewe and HSA reference models were obtained from SynergyFinder3. (A) BMS-536924 +
522 tyrphostin AG 1478, (B) BMS-536924 + AKT Inhibitor IV, (C) Temsirolimus + Akt Inhibitor
523 IV, (D) BMS-754807 + tyrphostin AG 1478, and (E) BMS-754807 + Akt Inhibitor IV. In each
524 plot, x and y axes represent drug concentrations. Red areas indicate synergy, while green areas
525 indicate antagonism. Black boxes highlight the MSA, with scores shown. Red circles in the top
526 right corner of each plot indicate the overall δ score. Color scales on the right of each plot show
527 the range of synergy scores. The data represented the average of three independent experiments
528 (n = 3).

529

530 **Table 3. Synergy scores for the secondary drug combinations (8×8 Matrix) in 2D cell models across four**
531 **reference models.**

Study	**Drug A**	**Drug B**	**Loewe δ score**		**HSA δ score**		**Bliss δ score**		**ZIP δ score**		**CSS %**
			Over-all	MSA	Over-all	MSA	Over-all	MSA	Over-all	MSA	
LWAS	Lapatinib	Doxorubicin	0.9	26.2	2.4	7.5	-3.4	-0.5	-2.8	1.6	71.4
	Lapatinib	Carboplatin	1.4	18.6	1.6	10.1	-4.1	1.2	-2.7	3.1	70.1
	Etoposide	Carboplatin	2.2	6.5	1.7	6.3	-1.9	2.7	-1.7	3.1	56.6
	Topotecan	Carboplatin	1.4	3.6	1.3	6.2	-3.4	1.1	-2.9	1.2	59.6
	Vincristine	Docetaxel	-1.4	--	0.7	5.2	-2.9	2.2	-2.5	3.5	68.8
	Gefitinib	Carboplatin	-1.4	7.5	2.3	8	-1.9	1.8	-1.3	2.7	55.6
	Cytarabine	Carboplatin	-4.4	5.9	3.2	9.2	-2.3	2.5	-2	0.1	65.0

GRR	AKTIV	Temsirolimus	6.1	12.1	7.9	16.4	1.3	4.8	1.4	5.3	58.6
	BMS-754807	Tyrphostin AG 1478	3.5	21.6	9	22.2	4.4	14.7	4.4	15.2	71.5
	BMS-754807	AKTIV	2.0	4.9	2.8	7.6	-1.3	1.9	-0.9	2.3	66.2
	BMS-536924	**Tyrphostin AG-1478**	**8.6**	**26.1**	**11.8**	**29.9**	**7.6**	**20.8**	**7.9**	**21.5**	**74.4**
	BMS-536924	AKTIV	5.4	10.3	5.7	16.3	1.9	6.7	2.3	7.2	79.3

Evaluation of selected GRR drug combinations for effects on SUM149 spheroids

To more accurately mimic IBC tumors, we utilized SUM149 spheroids as a 3D tumor model [33, 50]. In this assay, the SUM149 spheroids were allowed to form over 72 h before adding each of the three selected drug combinations identified from the 2D study. After an additional 72 h of treatment, cell viability was then evaluated using CellTiter-Glo, an ATP-based luminescence assay. To ensure consistency and allow direct comparison between 2D and 3D experiments, we used the same 8x8 dose-response matrix that was used in our 2D experiments.

In our 3D spheroid study the BMS-536924 and tyrphostin AG 1478 combination yielded overall synergy scores of (ZIP: 7.1, HSA: 12.2, Bliss: 6.9, and Loewe: 9.9), while MSA level scores were (ZIP: 11.8, HSA: 23.9, Bliss: 12.1, and Loewe: 17.9). BMS-536924 and AKTIV combination showed overall synergy scores of (ZIP: 4.1, Loewe: 0.5, Bliss: 3.4, and HSA: 7.8), with MSA level scores reaching (ZIP: 10.7, Loewe: 6.4, Bliss: 10.5, and HSA: 22.9). Lastly, for the temsirolimus and AKTIV combination, overall synergy scores were (ZIP:

548 6.1, Loewe: -8.2, Bliss: 5.8, and HSA: 7.7), with MSA level scores of (ZIP: 18.9, Loewe: 5.2,
549 Bliss: 18.2, and HSA: 19.9). The corresponding contour plots are shown in **Fig 6**. Based on the
550 accepted criteria of a synergy score exceeding 5 across all reference models [49], these results
551 indicate a synergistic effect at the MSA level for all tested combinations. Notably, as in the 2D
552 study, the BMS-536924 and tyrphostin AG 1478 combination also achieved synergy at the
553 overall level in the 3D study. It is worth noting that the Loewe model yielded a negative
554 synergy score for the combination of temsirolimus and AKTIV. This result may be attributed
555 to the fact that the Loewe model relies on well-defined dose-response curves for each agent
556 [51, 52], a condition not satisfied by temsirolimus in our 3D assay, where it failed to produce
557 a consistent dose–response relationship.
558
559 **Fig 6. Analysis of drug combinations in 3D SUM149 spheroid model.** Contour plots and
560 their synergy scores across Bliss, ZIP, Loewe and HSA reference models obtained from
561 SynergyFinder3. (A) BMS-536924 + tyrphostin AG 1478 (B) BMS-536924 + AKT Inhibitor
562 IV and (C) Temsirolimus + AKT Inhibitor IV combinations. In each plot, x and y axes represent
563 drug concentrations. Red areas indicate synergy, while green areas indicate antagonism. Black
564 boxes highlight the MSA, with scores shown. Red circles in the top right corner of each plot
565 indicate the overall δ score. Color scales on the right of each plot show the range of synergy
566 score. The data are represented as the average of three independent experiments (n = 3).
567
568 SynergyFinder+ was used to analyze the synergy scores and inhibition percentages (%)
569 based on percent-effect of DMSO control at specific concentrations. There was good
570 agreement between our 3D and 2D results, with comparable synergy scores across the four
571 reference models (**Table 4**). For the inhibition comparison, the BMS-536924 (1 μM) and
572 tyrphostin AG 1478 (0.1 μM) combination showed nearly identical % inhibition in both 2D

573 (78.6%) and 3D (79.1%) models. The BMS-536924 (1 μM) and AKTIV (1 μM) combination
574 was more effective in 3D, achieving 92.3% inhibition compared to 79.4% in 2D. The
575 temsirolimus (10 μM) and AKTIV (0.1 μM) combination achieved 61.2% inhibition in the 3D
576 model, which is comparable to the 54.2% inhibition observed in 2D (**S6 Fig**). The 3D results
577 also revealed stronger inhibitory effects from the combinations than from single agents. The
578 combination of BMS-536924 (1 μM) with Tyrphostin AG 1478 (0.1 μM) achieved 79.1%
579 inhibition, which is higher than each agent alone (BMS-536924: 66.6%; tyrphostin AG-1478:
580 3.7%). Similarly, combining BMS-536924 (1 μM) with AKTIV (1 μM) resulted in 92.3%
581 inhibition, surpassing the effects of individual treatments (BMS-536924: 65.1%; AKTIV:
582 73.1%). While the temsirolimus (10 μM) and AKTIV (0.1 μM) combination showed the lowest
583 inhibition (61.2%), it still demonstrated improved efficacy compared to single-agent treatments
584 (temsirolimus: -12.9%; AKTIV: 16.4%). Although the synergy metrics yielded high scores for
585 this combination (**Table 4**), those values can be misleading in the 3D context as these
586 calculations assume both drugs retain intrinsic activity, where their combined effect should be
587 greater than the additive expectation. However, temsirolimus showed minimal to no activity in
588 3D; therefore, this interaction might be better described as enhancement or potentiation of
589 AKTIV activity, which increased growth inhibition from 16.4 % with AKTIV alone to 61.2 %
590 in combination.

591 To further understand the effects of drug combinations on SUM149 spheroids, we used
592 the SYTOX™ Red Dead Cell Stain to visualize the spheroids using the IncuCyte system. In
593 all experimental panels, 0.2% DMSO was used as a negative (solvent) control, while
594 staurosporine (10 μM) was used as a positive inhibitor control [50], which, as expected, caused
595 significant spheroid disruption after 72 hours of treatment. The effects of individual drugs and
596 their combinations are shown in **Fig 7**. Some combinations, especially those involving BMS-
597 536924, appear to induce more pronounced changes in spheroid morphology compared to

598 single-agent treatments. The images reveal varying degrees of spheroid integrity and
599 morphological alterations in response to combination treatment.
600
601 **Fig 7. Representative SUM149 spheroids showing the effects of individual drugs and drug**
602 **combinations.** (A) BMS-536924 (1 μM) and tyrphostin AG-1478 (0.1 μM) combination. (B)
603 BMS-536924 (1 μM) and AKTIV (1 μM) combination. (C) Temsirolimus (10 μM) and AKTIV
604 (0.1 μM) combination. In each set, the top row shows spheroids at 0 h, while the bottom row
605 shows the same spheroids after 72 h of treatment. DMSO 0.2% represents a negative control
606 while staurosporine (10 μM) was used as a positive control.
607
608 **Table 4. Summary table of synergy scores in SUM149 2D and 3D cell models.**

Drug A	Drug B	Inhibition (%)						ZIP δ Score		HSA δ Score		Bliss δ Score		Loewe δ Score	
		2D			3D										
		Com	A	B	Com	A	B	2D	3D	2D	3D	2D	3D	2D	3D
BMS-536924 (1 μM)	Tyrphostin AG-1478(0.1 μM)	79	30	28	79	67	3.7	31	12	49	13	30	11	34	15
BMS-536924 (1 μM)	AKTIV (1 μM)	79	27	48	92	65	73	12	6	32	19	17	1.6	19	19
AKTIV (0.1 μM)	Temsirolimus (10 μM)	54	6.5	39	61	16	13	9.6	46	15	45	11	56	16	42

609
610 Data were derived from bar plots generated by SynergyFinder+ software and represent the average of three
611 independent experiments (**S6 Fig**). The table shows the percent inhibition for the drug combinations (Com), and

612 drugs alone at their respective concentrations, along with the synergy scores calculated using four different
613 models: ZIP, HSA, Bliss, and Loewe for each combination. All synergy scores above five indicate a synergistic
614 effect, with higher values suggesting stronger synergy.
615
616 Taken together, the drugs we identified from both the 2D and 3D combination screening
617 pipeline included inhibitors BMS-536924 [53] targeting IGF1-R, tyrphostin AG-1478 [54, 55]
618 targeting EGFR, Akt inhibitor IV [56] targeting Akt phosphorylation, and temsirolimus [57]
619 targeting mTOR.
620

621 Assessment of selected GRR drug combinations on SUM149 622 motility

623 To evaluate the identified drugs for effects on cell migration, a critical parameter in
624 cancer cell behavior and metastasis, we used the "wound healing" assay, utilizing IncuCyte's
625 precision WoundMaker tool. For this assay, a wound is created within a confluent cell
626 monolayer, and cell movement back into the wound measured in real time using automated
627 IncuCyte imaging. Cells were plated overnight and then the "wound" was created, followed by
628 selected combination drug treatments (as listed in **Table 4**). Relative Wound Density (RWD)
629 %, which considers any effects of cell proliferation, was calculated to quantify cell movement
630 into the wound area relative to initial wound size over 24 h.
631 The DMSO vehicle control demonstrated progressive wound closure over the 24 h
632 observation period (shown in **Fig 8**). SUM149 treatment with the IGF1-R inhibitor BMS-
633 536924 (1 μM) did not result in any significant effect on migration kinetics compared to control
634 ($p > 0.05$), while treatment with the mTOR inhibitor tyrphostin AG-1478 (0.1 μM) had a
635 significant effect on slowing wound closure with $p < 0.05$. When both BMS-526924 and
636 tyrphostin AG-1478 were combined at those concentrations, migration was significantly

637 reduced by 30% at 24 h ($p < 0.001$). The combination treatment was not significantly different
638 from tyrphostin AG-1478 treatment alone. SUM149 cells treated with the Akt inhibitor AKTIV
639 (1 μM) had significantly impaired wound closure, reducing migration by > 50% compared to
640 control at 24 h ($p < 0.001$). When both BMS-526924 and AKTIV were combined at these
641 concentrations, migration was reduced by 30% at 24 h ($p < 0.001$). The combination treatment
642 was not significantly different from AKTIV treatment alone. Treatment of SUM149 cells with
643 temsirolimus (1 μM), an mTOR complex 1 inhibitor, significantly reduced migration by ~ 40%
644 relative to control at 24 h ($p < 0.05$). The combination of temsirolimus and low dose AKTIV
645 (0.1 μM) did produce significant effects ($p < 0.001$) compared to the control and single
646 treatments. Representative wound healing images and corresponding statistical analyses are
647 shown in **Fig 8**, with each experimental condition performed in eight replicates (n = 8).
648
649 **Fig 8. Effect of GRR selected drugs on SUM149 motility.** Relative wound density (RWD
650 %) was measured at 6 h intervals from 0 to 24 h. The effects of individual drugs and their
651 combinations are compared to the DMSO control. (A) Representative images of wound closure
652 over 24 h treatment for each condition. (B) to (D) Quantification of the RWD % relative to
653 each combination. (B) BMS 536924 (1 μM) and tyrphostin AG 1478 (0.1 μM). (C) BMS
654 536924 (1 μM) and AKTIV (1 μM). (D) Temsirolimus (10 μM) and AKTIV (0.1 μM).
655 Statistical significance is indicated by asterisks (*p < 0.05, **p < 0.01, ***p < 0.001, ****p <
656 0.0001, ns: not significant). Error bars represent mean ± SEM from eight technical replicates.
657

658 **Selected GRR combinations mediate the reduction of**
659 **phosphoprotein expression**

660 We next evaluated the effects of the selected three drug combinations on key signaling
661 proteins in SUM149 cells. The analysis focused on expression levels and phosphorylation
662 status of Akt, EGFR, IGF1-R, and mTOR proteins in response to single- and combination-drug
663 treatments. Western blot analysis was performed after 24 h of drug treatment, and
664 densitometric analysis for all treatment conditions, including individual drugs and
665 corresponding combinations, and representative blots are presented in **Fig 9**. Densitometric
666 analyses of triplicate experiments (representative whole blots shown in **S7 Fig**) confirmed the
667 statistical significance of these phosphorylation changes, with β-actin serving as the loading
668 control across all conditions. The maintenance of total protein levels across treatments suggests
669 that the observed effects were specific to protein phosphorylation rather than overall protein
670 expression. Due to technical challenges using the Li-COR system for IGF1-R and pIGF1-R,
671 HRP-tagged secondary antibodies and iBRIGHT imaging was used for these proteins (**S7 Fig**).
672 All four of the proteins targeted by our selected GRR combinations were detectable in the
673 SUM149 IBC cell line by Western blot (**Fig 9**), and the drug combinations effectively
674 suppressed their target pathways (**Fig 9** and **S7 Fig**). The combination of AKTIV (0.1 μM)
675 with temsirolimus (10 μM) demonstrated the strongest inhibitory effects, achieving a
676 significant reduction of both p-Akt ($p < 0.001$) and p-mTOR ($p < 0.01$) (**Fig 9A**). The second
677 combination, AKTIV (1 μM) with BMS-536924 (1 μM), showed a significant decrease in p-
678 Akt levels ($p < 0.01$) (**Fig. 9B**), which appeared to be primarily driven by BMS-536924 rather
679 than AKTIV. The combination of tyrphostin AG-1478 (0.1 μM) and BMS-536924 (1 μM)
680 resulted in a reduction in both phosphorylated EGFR (p-EGFR) levels and phosphorylated
681 IGF1-R (p-IGF1-R), but did not meet statistical significance, while maintaining stable total
682 protein levels for EGFR and IGF1-R (**Fig. 9C**).

683

684 **Fig 9. Western blot analysis of protein expression levels in response to the tested drugs**
685 **and combinations.** Representative Western blots for (A) Temsirolimus (10 μM) and Akt
686 inhibitor IV (0.1 μM) combination effects on the expression of p-Akt, total Akt, p-mTOR, and
687 total mTOR; (B) Akt Inhibitor IV (1 μM) and BMS-536924 (1 μM) combination effects on the
688 expression of p-Akt, total Akt, p-IGF1-R, and total IGF1-R; and (C) Tyrphostin AG-1478 (0.1
689 μM) and BMS-536924 (1 μM) combination effects on the expression of p-EGFR, total EGFR,
690 p-IGF1-R, and total IGF1-R. The presence (+) or absence (-) of each treatment is indicated,
691 with β-actin serving as a loading control. Quantification of DMSO bands vs each treatment
692 bands. Representative whole-blot images of triplicate samples (n = 3) are shown in **S7 Fig**.

693

694 Assessment of differential gene expression changes in SUM149
695 cells treated with the selected GRR combinations.

696 To assess if the selected GRR combinations we identified herein with efficacy in
697 multiple IBC cell models significantly reversed IBC gene expression, we undertook a RNA
698 Seq analysis. For this, SUM149 cells were cultured and treated for 24 h (n = 3) with the selected
699 GRR combinations, as well as DMSO vehicle control. RNA was isolated and RNA-Seq
700 conducted as in materials and methods. All three combination treatments caused significant
701 global gene expression changes in SUM149 (see heatmaps and volcano plots in **S8 Fig**).
702 Analysis of the expression of the 297 IBC-GES genes only in SUM149 cells treated with the
703 three dual-drug combinations revealed distinct transcriptional reversal patterns. For those IBC-
704 GES genes detected as significantly expressed ($p$adj < 0.05) in SUM149 cells (blue columns
705 in **Fig 10**), the combinations BMS-536924 + AKTIV, BMS-536924 + tryrphostin, and
706 temsirolimus + AKTIV, reversed 50%, 52% and 48% of the IBC-GES genes detected,
707 respectively (orange columns **Fig 10**).

708

709 **Fig 10. IBC gene expression signature changes induced by GRR combinations in SUM149**
710 **cells.** SUM149 cells were incubated with GRR combinations or DMSO alone for 24 h, and
711 RNA isolated for RNA-Seq analysis (n = 3 biological replicates). Left: DMSO (0.2%) vs
712 (BMS-536924 (1 μM) + AKTIV (1 μM)); middle: DMSO (0.2%) vs (BMS-536924 (1 μM)) +
713 tyrphostin AG1478 (0.1 μM)); right: DMSO (0.2%) vs (AKTIV (0.1 μM) + temsirolimus (10
714 μM)). Data was analyzed to identify genes significantly expressed in SUM149 cells (*p*adj <
715 0.05). Data are plotted as number of IBC-GES genes: detected in SUM149 cells (blue
716 columns), number of detected IBC-GES genes reversed by the combination treatment (orange
717 columns), and the number reversed up (green columns) and reversed down (purple columns).

718 # Discussion

719 Due to the limited availability of therapies targeting IBC, particularly for the triple-
720 negative (TNBC) subtype, there is a critical need to identify novel targets and drugs to halt its
721 rapid progression and aggressive metastasis [2, 58]. Drug repurposing is one approach to
722 identify therapies for rare diseases such as IBC [22, 24, 59]. We have previously used two
723 computational approaches: text mining (LWAS) and gene expression reversal rate analysis
724 (GRR), as predictive tools for identifying novel drug candidates for IBC [27, 28].

725 To gauge the predictive value of our computational approaches for identifying new
726 drugs to repurpose for IBC, we tested the drugs and compounds for anti-proliferative efficacy
727 in four breast cancer cell lines, including SUM149, an IBC model. The oncology-focused
728 LWAS method [27], showed a higher success rate, with 17 of 24 compounds (70%)
729 demonstrating efficacy in the cell line models. For the GRR approach, which had identified
730 both non-oncology and oncology drugs [28], the success rate was lower, with 6 out of 16
731 compounds (~38%) showing efficacy in the cell line models. Among the LWAS-predicted
732 drugs for IBC, paclitaxel, docetaxel, and doxorubicin showed the highest efficacy with
733 nanomolar IC_{50} potencies in SUM149 (**Tables 1 and 5**). These drugs are FDA-approved for
734 breast cancer and are also among those used as IBC treatment options [14]. All 11 of the LWAS
735 drugs that have been tested in clinical trials for IBC (**S1 Table**), showed efficacy in our
736 SUM149 Hoechst assay. Of the other 13 LWAS drugs/compounds not yet tested in clinical
737 trials for IBC (**S1 Table**), 6 demonstrated activity in our SUM149 Hoechst assay (46%
738 success), while 7 showed no activity. For the 7 with no activity, there were no reports on these
739 drugs having activity in IBC models. Four novel drug candidates with in vitro efficacy were
740 identified, which, to our knowledge, had not previously been investigated for IBC (as
741 determined from a review of PubMed and clinicaltrials.gov (**S1 Table**)). These included
742 topotecan, a topoisomerase I inhibitor, and cytarabine, an antimetabolite, which had potency

743 across all tested cell lines, including IC_{50} values of 0.008 μM and 0.025 μM in SUM149,
744 respectively. In our initial computational LWAS analysis [27], topotecan appeared among the
745 drugs linked to medulloblastoma, while cytarabine was associated with acute lymphocytic
746 leukemias, both diseases that clustered closely to IBC [27]. This semantic co-occurrence
747 analysis suggests that other drugs targeting these "IBC-clustered" diseases, such as
748 daunorubicin and vincristine, would also have activity in IBC models, and we did observe
749 efficacy for these two drugs *in vitro* (**Table 5**).
750
751 **Table 5. Clinical status of LWAS-predicted drug candidates in IBC.**

Drug Class	**Drug Name** [a]	**Activity in SUM149** [b]	**Clinical Trials for IBC** [c]	**Treatment Option for IBC** [d]
Vinca Alkaloids	Vincristine	+ + + +	No	No
	Vinorelbine	+ +	Yes	Yes
Antimetabolites	Methotrexate	+	Yes	Yes
	5-Fluorouracil	+	Yes	Yes
	Gemcitabine	+ + + +	Yes	Yes
	Hydroxyurea	-	No	No
	Cytarabine	+ + +	No	No
Alkylating Agents	Carmustine	-	No	No
	Ifosfamide	-	No	No
	Dacarbazine	-	No	No
	Carboplatin	+	Yes	Yes
Anthracyclines	Daunorubicin	+ + + +	No	No
	Doxorubicin	+ + + +	Yes	**Yes**
Topoisomerase Inhibitors	Etoposide	+ + +	Yes	No
	Mitoxantrone	+ + + +	No	No
	Topotecan	+ + + +	No	No
Taxanes	Paclitaxel	+ + + +	Yes	**Yes**

	Docetaxel	+ + + +	Yes	**Yes**
Kinase Inhibitors	Gefitinib	+ + +	No	No
	Imatinib	-	No	No
	Sunitinib	+ +	Yes	No
	Lapatinib	+ +	Yes	Yes
Peptide drug	Octreotide	-	No	No
Glucocorticoid	Prednisone	-	No	No

[a] From Ji et al. 2020 [27]). [b] Activity data for drug in SUM149 (based on Table 1 in the current study; from minimal [-] to high activity [++++]. [c] Tested in clinical trials (clinicaltrials.gov). [d] American Cancer Society, Chainitikun et al. [17], and MD Anderson Cancer Center's IBC Treatment Algorithm [45].

TKIs, such as lapatinib, gefitinib, and sunitinib, showed varying potency and efficacy against SUM149, with gefitinib having the lowest IC_{50} value of 0.4 μM, and lapatinib achieving the highest efficacy ~ 90%, at 10 μM. These two drugs target EGFR, which is highly expressed in the SUM149 cell line [60, 61], and, along with the finding that EGFR signaling plays a role in IBC progression and metastasis and can be blocked by EGFR inhibition [62], likely explains the effectiveness of these drugs in SUM149. While lapatinib has been tested clinically for IBC and showed limited success [63, 64], adverse events and toxicity were observed [17, 65], and there are currently no ongoing clinical trials for lapatinib.

Our validation of the GRR list identified novel effective drugs previously untested against IBC, primarily TKIs targeting multiple downstream pathways. Notably, tipifarnib, a farnesyltransferase inhibitor (FTI), demonstrated the highest potency (IC_{50} = 0.08 μM) in SUM149. This finding aligns with the contributing role of RhoC GTPase, a Ras superfamily member, in IBC pathogenesis [66, 67]. Since RhoC activation requires farnesylation, a post-translational modification, it can be targeted by FTIs. Tipifarnib has also progressed to Phase II clinical trials in locally advanced breast cancer (LABC), both as monotherapy and in

771 combination with hormonal therapy [66, 67]. These results validate our approach and support
772 the potential of other GRR effective compounds as repurposed therapeutic candidates for IBC
773 treatment.

774 The IGF1-R inhibitors BMS-754807 and BMS-536924 showed IC_{50} values of 0.5 μM
775 and 1.9 μM in the Hoechst assay, respectively. Differences in potency may be attributed to
776 BMS-536924's selective binding characteristics compared to BMS-754807's broader IGF1-
777 R/IR inhibition profile [68, 69]. BMS-536924 has previously been shown to have anti-growth
778 activity in SUM149 and MCF7 cells [70]. While these IGF1-R inhibitors have been tested in
779 preclinical breast cancer models [69, 71] and in clinical trials for breast cancer [72], they remain
780 unexplored in clinical trials for IBC, suggesting potential novel therapeutic opportunities,
781 although there are no FDA-approved small-molecule inhibitors of IGF1-R. Temsirolimus, an
782 mTORC1 inhibitor [57], showed moderate potency for cytotoxicity in SUM149 (absolute IC_{50}
783 = 4.3 μM), but a high potency for proliferation (relative IC_{50} = 0.1 nM). While FDA-approved
784 for renal cell carcinoma, and assessed in clinical trials for metastatic breast cancer [73],
785 temsirolimus has not been specifically investigated for IBC treatment, presenting an additional
786 therapeutic avenue worth exploring both as monotherapy or in combinations. Another mTOR
787 inhibitor, everolimus, which did not show up in our GRR analysis, has been FDA-approved for
788 some types of metastatic breast cancer [74, 75]. Tyrphostin AG 1478, an EGFR inhibitor [54,
789 55], and AKTIV [56, 76] showed comparable potency with IC_{50} values of 0.23 μM in SUM149
790 cells, yet neither has been evaluated for IBC treatment. These results suggest promising
791 therapeutic potential for expanding treatment options in IBC, with the possibility of evaluating
792 additional FDA-approved EGFR inhibitors and the approved Akt inhibitor, both as single
793 agents and in combination. The mechanisms of action for the effective LWAS and GRR
794 candidates, as well as corresponding pathways, are illustrated in **Fig 11**.
795

796 **Fig 11. Cellular signaling pathways targeted by effective drugs previously identified**
797 **through computational approaches.** (A) LWAS 17 effective compounds, representing
798 diverse drug classes. These include targeted therapies such as tyrosine kinase inhibitors (TKIs)
799 and different chemotherapeutic agents categorized by their mechanisms: microtubule-targeting
800 drugs, DNA-damaging agents (e.g., topoisomerase I and II inhibitors), platinum-based drugs,
801 and antimetabolites. (B) GRR 6 effective compounds, all of which are TKIs, targeting various
802 receptors and their downstream signaling pathways such as RAS/RAF/MEK/ERK and
803 PI3K/AKT/mTOR. These pathways regulate critical cellular processes, including proliferation,
804 differentiation, cell cycle, invasion, and epithelial-mesenchymal transition (EMT).

805 Due to challenges with single-drug approaches in cancer therapy, including drug
806 resistance, we also examined drug combinations targeting multiple pathways. We focused on
807 the most promising synergistic drug combinations identified in our initial screening. Further,
808 due to the reported limitations of 2D cultures in identifying clinically relevant drug treatments,
809 we also tested the synergistic combinations in 3D SUM149 tumor models [50], aiming to
810 mimic the tumor architecture more accurately. We used a high-throughput approach to first
811 screen combinations at single dose and then in a more extensive 8x8 matrix (**Fig 3**). A
812 comparable approach to identify novel drug combinations with synergy for other cancers has
813 been reported [77]. Our initial combinations were carried out by evaluating each drug at its
814 EC_{25} concentration, with the Bliss method used to calculate Bliss excess scores. This resulted
815 in identifying 25 combinations from the LWAS list and 9 combinations from the GRR list (p
816 < 0.05). Then, we performed an 8×8 matrix analysis focusing on combinations with the highest
817 Bliss excess scores. Our synergy analysis using SynergyFinder3 revealed three synergistic
818 combinations meeting our stringent criteria, with scores greater than 5 across all reference
819 models (Bliss, Loewe, HSA, and ZIP) at the MSA level. SynergyFinder+ was used to confirm
820 these results at the micro visualization scale, with detailed bar plots presented in **S6 Fig**.

821 Interestingly, all three combinations originate from the GRR list that involves novel targeted
822 compounds for IBC treatment. Four targeted agents were prominent within these identified
823 combinations: BMS-536924 [53], AKTIV [56, 76], tyrphostin AG-1478 [54, 55], and
824 temsirolimus [57]. Each of these drugs targets specific nodes within the PI3K/Akt/mTOR
825 signaling cascade, supporting their potential in addressing the aggressive characteristics of
826 IBC.

827 Our synergyfinder+ analysis on a micro visualization scale identified three synergistic
828 combinations: termed our selected GRR combinations. The combinations include EGFR
829 inhibitor, IGF1-R/IR inhibitor, Akt inhibitor, and mTOR inhibitor that can directly or indirectly
830 target different components of the PI3K/Akt/mTOR pathway (**Fig 12**) a crucial signaling
831 cascade in several cancers [78-80].

832

833 **Fig 12. Schematic representation of PI3K/AKT/mTOR downstream signaling pathway**
834 **targeted by the selected GRR combinations.** The diagram shows the crosstalk between
835 EGFR and IGF1-R with the PI3K/AKT/mTOR pathway to regulate the cell cycle. The three
836 GRR drug combinations are highlighted: tyrphostin AG-1478 + BMS-536924, AKT inhibitor
837 IV + BMS-536924, and AKT inhibitor IV + temsirolimus.

838

839 The first combination of BMS-536924 (1 μM) and tyrphostin AG-1478 (0.1μM) stands
840 as a novel and promising approach, yielding the highest synergy score in both the primary
841 combination screening with Bliss excess score = -0.266 as well as the secondary combination
842 matrix screening in 2D and 3D models (Synergy scores summarized in **Table 4**). This
843 combination primarily targets the crosstalk between EGFR and IGF1-R [81]. High levels of
844 IGF-1R can cause resistance across different cancers [72, 82], and cancer cells can become
845 resistant to IGF-1R inhibitors, by activating PI3K/mTOR pathways through alternative EGFR

signaling [83, 84]. It was also reported that the interaction between IGF-1R and different receptor tyrosine kinases, such as EGFR, can create complex compensatory mechanisms that can limit treatment efficacy and promote resistance when targeting individual pathways [85]. These interactions occur through multiple mechanisms, including direct receptor associations and downstream signaling networks [86]. These compensatory mechanisms provide a strong rationale for dual targeting of both EGFR and IGF-1R with a consideration of reducing the cytotoxicity of the combined drugs by using the lowest concentrations that can achieve high synergy scores.

The IGF1-R/Akt signaling crosstalk represents a promising therapeutic target, addressed by our second identified drug combination of BMS-536924 (1 μM) and AKTIV (1 μM). Akt, also known as protein kinase B, mediates signal transduction from receptor tyrosine kinases, including IGF1-R and IR, via the PI3K pathway. This signaling cascade promotes G1/S cell cycle transition, which is crucial for cellular proliferation [78, 87]. The significant overlap between IGF1-R and Akt signaling provides a mechanistic rationale for the simultaneous targeting of both molecules.

Our studies identified another combination, temsirolimus (10 μM) and AKTIV (0.1 μM), that can simultaneously target mTOR and Akt. mTOR, a downstream effector, functions as a central regulatory kinase that operates multiple essential cellular survival processes through two different protein complexes: mTORC1 and mTORC2. Through these complexes, mTOR can execute its regulatory functions by phosphorylating key downstream proteins, including Akt [88, 89]. We suggest that targeting both proteins through our identified combination of temsirolimus, an mTORC1 inhibitor [57, 90], alongside AKTIV may effectively reduce the likelihood of drug resistance development while achieving more complete pathway suppression. Capivasertib was recently approved by FDA as the first Akt inhibitor drug for treating hormone receptor (HR)-positive, human epidermal growth

871 factor 2 (HER2)-negative advanced or metastatic breast cancer [91, 92]. This approval
872 validates Akt as a promising clinical target and supports our findings that Akt inhibitors, which
873 appeared in two of the three identified combinations, could be potentially effective in treating
874 IBC.

875 We also tested all the selected combinations in 3D cell models. Although all these
876 combinations showed synergistic effects at the proliferation level in 2D, the temsirolimus and
877 AKTIV combination showed a significant shift in 3D cell models, where temsirolimus loses
878 its single-agent efficacy. This phenomenon may represent a mechanistic transition from
879 classical synergy observed in 2D cultures (where both agents demonstrate independent
880 activity) to a potentiator or enhancer effect in 3D models, as described previously [93]. While
881 temsirolimus alone appeared to be ineffective, it significantly sensitized cells to AKTIV,
882 enhancing the growth inhibition from 16.4% as an AKTIV single agent to 61.2% in
883 combination. Mechanistically, this transition reflects fundamental aspects of 3D tumor biology,
884 where cells in spheroids can activate survival pathways (e.g., mTOR), which has been reported
885 to have a greater effect on survival in 3D than in 2D breast cancer cell cultures and may
886 contribute to drug resistance [94]. This shift allows for more accurate modeling of tumor
887 behavior and drug responses, making 3D cultures a valuable tool in cancer research and drug
888 development. This could potentially be translated to enhance therapeutic efficacy in clinical
889 applications, particularly in IBC, where these pathways are known to drive tumor growth and
890 survival [2, 16].

891 To investigate how these drug combinations might affect IBC cell migration, we
892 performed wound-healing assays to assess drug effects on cell motility. Our results
893 demonstrated that the combinations of (BMS-536924 + tyrphostin AG-1478) and
894 (temsirolimus + AKTIV) enhanced the inhibitory effects of the individual drugs on cell motility
895 and migration. This aligns with studies reporting the role of the PI3K/Akt/mTOR pathway in

896 cell motility/invasion, and its crosstalk with IGF1-R and EGFR signaling, either in SUM149
897 [95, 96] or in TNBC [97-100]. In our study, the combination co-targeting Akt upstream (by
898 AKTIV) and mTORC1 downstream (by temsirolimus) may effectively shut down the
899 PI3K/Akt/mTOR axis and prevent any compensatory rebound activation. In essence, Akt
900 inhibition blocks the bulk of signaling through the pathway, while mTORC1 inhibition ensures
901 that any Akt activity not fully suppressed (or any Akt-independent mTOR activation) is also
902 blocked. These results demonstrate that effective suppression of cell migration in SUM149
903 requires a multi-targeted approach, given the interconnected nature of growth factor receptor
904 signaling, and involves the PI3K/Akt/mTOR pathway.

905 We also assessed the GRR combinations for direct effects on signaling pathways in
906 SUM149 cells, and we observed that the combination of AKTIV and temsirolimus suppressed
907 phosphorylation of both Akt and mTOR (**Fig. 9A**). While temsirolimus appeared to be the
908 primary driver of this suppression, the combination showed enhanced suppressive effects
909 compared to control, indicating potential synergistic interactions within the Akt/mTOR
910 signaling pathway. The combination of AKTIV and BMS-536924 also suppressed Akt
911 phosphorylation, predominantly by BMS-536924 (**Fig. 9B**). While IGF1-R phosphorylation
912 trended lower with AKTIV and BMS-536924 treatment, it did not reach significance due to
913 some variability across experiments. This was also complicated by our observation that BMS-
914 536924 appeared to increase total IGF1-R expression, perhaps indicating the activation of
915 compensatory mechanisms in response to pathway inhibition, as reported previously [101,
916 102]. While in cell-based efficacy assays, AKTIV demonstrated anti-proliferative effects with
917 an IC_{50} of 0.2 μM, both 1 μM and 0.1 μM, AKTIV did not appear to reduce p-Akt expression,
918 perhaps due to differences in assay timing (24 h for Western blot compared to 72 h for the cell
919 assays), or indicating an off-target effect in the cell assays. In the BMS-536924 + tyrphostin

920 combination (**Fig. 9C**), although not significant, pEGFR and pIGFR levels trended lower
921 compared to controls.

922 The gene reversal approach involves identifying drugs capable of reversing disease-
923 associated gene expression signatures back to a 'normal/healthy' transcriptomic state [31]. In
924 our previous computational GRR study, we had first generated a 387 IBC-gene expression
925 signature (IBC-GES) compiled from published studies using IBC patient samples (see citations
926 in [28]). 297 of these 387 genes had drug data in the LINCS database, and our GRR analysis
927 [28] identified drug perturbations that significantly reversed the expression of genes in the IBC-
928 GES list. For example, tyrphostin AG-1478 had a GRR score of 59% [28], meaning 175 of the
929 297 genes were reversed. In our RNA-Seq study herein assessing the three drug combinations
930 in SUM149 cells, ~half of the detectable IBC-GES genes were reversed in expression by the
931 drug combinations, suggesting some reprogramming of IBC-associated transcriptional
932 profiles.

933 An assessment of the global gene expression changes in our RNA-Seq data identified
934 significant downregulation of cell cycle regulators, DNA replication enzymes, and survival
935 factors across all treatment groups. For example, both BMS-536924 + tyrphostin and the BMS-
936 536924 + AKTIV treatments reduced expression of RRM2, a key driver of DNA synthesis and
937 proliferation. RRM2, which encodes ribonucleotide reductase, is overexpressed in aggressive
938 basal-like and TNBC, where elevated levels correlate with adverse clinical features including
939 larger tumor burden, lymph node involvement, and disease recurrence [103, 104]. Another
940 gene, cyclin E2 (CCNE2) was found to be downregulated by two combinations: AKTIV +
941 temsirolimus and BMS-536924 + AKTIV. CCNE2, an S phase cyclin is frequently
942 overexpressed in breast cancer [105] with previous studies reported the overexpression of
943 Cyclin E including CCNE2 in IBC, with correlation of poor prognosis in IBC patients [106].

All these results highlight the therapeutic promise of the identified combinations in combating IBC, and to our knowledge, we are the first to report these novel combinations. The three most effective combinations all came from drugs identified in the GRR computational analysis emphasizing the need for multiple approaches to identify effective novel combinations. While these initial findings are promising, significant studies are still needed to examine their long-term efficacy, potential resistance mechanisms, and validation in additional IBC models and patient-derived samples before advancing to clinical trials.

Conclusions

This study bridges the gap between computational predictions and experimental validation in drug repurposing for IBC. Our findings validate the potential of our *in-silico* approaches and identified novel, potentially synergistic drug combinations that require further exploration for IBC treatment. By combining computational methods with experimental validation, we have opened new avenues for IBC therapy that could enhance therapeutic responses for individuals affected by this aggressive breast cancer subtype. Future research directions will be needed to validate the identified drug combinations in additional IBC cell models beyond SUM149 as well as *in vivo* studies to assess the different combination's therapeutic efficacy, establish optimal dosing regimens, and characterize toxicity profiles in a physiologically relevant context. This systematic approach aimed to uncover novel IBC-specific therapeutic targets that could lead to new effective treatment strategies.

Author Contributions

Conceptualization, K.P.W., X.J. and W.Z.; methodology, E.A.S., M.T., and X.J..; software, E.A.S. and J.E.S.; formal analysis, E.A.S., J.E.S. and K.P.W.; investigation, EA.S., M.T. and X.J.; writing—original draft preparation, K.P.W., J.E.S. and E.A.S.; writing—review and editing, E.A.S., X.J., M.T., M.S.D., W.Z., J.E.S. and K.P.W.; visualization, E.A.S.; supervision, K.P.W. and J.E.S.; funding acquisition, K.P.W. All authors have read and agreed to the published version of the manuscript.

Funding

This research was supported by National Institutes of Health, grants U54MD012392 (RCMI Program at NCCU), R01MD017405, R01AA026068 and U54AA030451. Additional funding was from Golden LEAF Foundation and the BIOIMPACT Initiative of the State of North Carolina through the Biomanufacturing Research Institute & Technology Enterprise (BRITE) Center for Excellence at North Carolina Central University.

Data Availability Statement

The raw data supporting the conclusions of this article will be made available by the authors on request.

Acknowledgements

Schematic and Pathway Figures, and graphical abstract were created with BioRender.com.

Conflicts of Interest

The authors declare no conflicts of interest.

References

1. Fouad TM, Kogawa T, Liu DD, Shen Y, Masuda H, El-Zein R, et al. Overall survival differences between patients with inflammatory and noninflammatory breast cancer presenting with distant metastasis at diagnosis. Breast cancer research and treatment. 2015;152:407-16.

2. Lim B, Woodward WA, Wang X, Reuben JM, Ueno NT. Inflammatory breast cancer biology: the tumour microenvironment is key. Nature Reviews Cancer. 2018;18(8):485-99.

3. Robertson FM, Bondy M, Yang W, Yamauchi H, Wiggins S, Kamrudin S, et al. Inflammatory breast cancer: the disease, the biology, the treatment. CA: a cancer journal for clinicians. 2010;60(6):351-75.

4. Abraham HG, Xia Y, Mukherjee B, Merajver SD. Incidence and survival of inflammatory breast cancer between 1973 and 2015 in the SEER database. Breast Cancer Research and Treatment. 2021;185:229-38.

5. Hester RH, Hortobagyi GN, Lim B. Inflammatory breast cancer: early recognition and diagnosis is critical. American journal of obstetrics and gynecology. 2021;225(4):392-6.

6. Hance KW, Anderson WF, Devesa SS, Young HA, Levine PH. Trends in inflammatory breast carcinoma incidence and survival: the surveillance, epidemiology, and end results program at the National Cancer Institute. Journal of the National Cancer Institute. 2005;97(13):966-75.

7. Boussen H, Bouzaiene H, Hassouna JB, Gamoudi A, Benna F, Rahal K, editors. Inflammatory breast cancer in Tunisia: reassessment of incidence and clinicopathological features. Seminars in oncology; 2008: Elsevier.

8. Dawood S, Ueno NT, Valero V, Woodward WA, Buchholz TA, Hortobagyi GN, et al. Differences in survival among women with stage III inflammatory and noninflammatory

1008 locally advanced breast cancer appear early: a large population‐based study. Cancer.
1009 2011;117(9):1819-26.
1010 9. Luo Y, Li Q, Fang J, Pan C, Zhang L, Xu X, et al. ER+/PR− phenotype exhibits more
1011 aggressive biological features and worse outcome compared with ER+/PR+ phenotype in
1012 HER2-negative inflammatory breast cancer. Scientific Reports. 2024;14(1):197.
1013 10. Matro JM, Li T, Cristofanilli M, Hughes ME, Ottesen RA, Weeks JC, et al.
1014 Inflammatory breast cancer management in the national comprehensive cancer network: the
1015 disease, recurrence pattern, and outcome. Clinical breast cancer. 2015;15(1):1-7.
1016 11. Jagsi R, Mason G, Overmoyer BA, Woodward WA, Badve S, Schneider RJ, et al.
1017 Inflammatory breast cancer defined: proposed common diagnostic criteria to guide treatment
1018 and research. Breast Cancer Res Treat. 2022. Epub 2022/01/02. doi: 10.1007/s10549-021-
1019 06434-x. PubMed PMID: 34973083.
1020 12. Yamauchi H, Woodward WA, Valero V, Alvarez RH, Lucci A, Buchholz TA, et al.
1021 Inflammatory breast cancer: what we know and what we need to learn. The oncologist.
1022 2012;17(7):891-9.
1023 13. Dawood S, Merajver S, Viens P, Vermeulen P, Swain S, Buchholz T, et al.
1024 International expert panel on inflammatory breast cancer: consensus statement for
1025 standardized diagnosis and treatment. Annals of oncology. 2011;22(3):515-23.
1026 14. Newman AB, Lynce F. Tailoring treatment for patients with inflammatory breast
1027 cancer. Current Treatment Options in Oncology. 2023;24(6):580-93.
1028 15. Rueth NM, Lin HY, Bedrosian I, Shaitelman SF, Ueno NT, Shen Y, et al. Underuse
1029 of trimodality treatment affects survival for patients with inflammatory breast cancer: an
1030 analysis of treatment and survival trends from the National Cancer Database. Journal of
1031 Clinical Oncology. 2014;32(19):2018-24.

1032 16. Wang X, Semba T, Phi LTH, Chainitikun S, Iwase T, Lim B, et al. Targeting
1033 signaling pathways in inflammatory breast cancer. Cancers. 2020;12(9):2479.
1034 17. Chainitikun S, Saleem S, Lim B, Valero V, Ueno NT. Update on systemic treatment
1035 for newly diagnosed inflammatory breast cancer. Journal of Advanced Research. 2021;29:1-
1036 12.
1037 18. Wilkinson GF, Pritchard K. In vitro screening for drug repositioning. Journal of
1038 biomolecular screening. 2015;20(2):167-79.
1039 19. Schuler J, Falls Z, Mangione W, Hudson ML, Bruggemann L, Samudrala R.
1040 Evaluating the performance of drug-repurposing technologies. Drug discovery today.
1041 2022;27(1):49-64.
1042 20. Zong N, Wen A, Moon S, Fu S, Wang L, Zhao Y, et al. Computational drug
1043 repurposing based on electronic health records: a scoping review. NPJ digital medicine.
1044 2022;5(1):77.
1045 21. Pillai M, Wu D, editors. Validation approaches for computational drug repurposing: a
1046 review. AMIA Annual Symposium Proceedings; 2023: American Medical Informatics
1047 Association.
1048 22. Zhang Z, Zhou L, Xie N, Nice EC, Zhang T, Cui Y, et al. Overcoming cancer
1049 therapeutic bottleneck by drug repurposing. Signal transduction and targeted therapy.
1050 2020;5(1):113.
1051 23. Dhanush Y, Ganesh VS. Non-oncologic to oncologic drug: A systematic review of
1052 drug repurposing in cancer. Cancer Chemotherapy and Pharmacology. 2025;95(1):91.
1053 24. Ko Y. Computational drug repositioning: current progress and challenges. Applied
1054 Sciences. 2020;10(15):5076.
1055 25. Chen B, Butte A. Leveraging big data to transform target selection and drug
1056 discovery. Clinical Pharmacology & Therapeutics. 2016;99(3):285-97.

1057 26. Khanjani F, Jafari L, Azadiyan S, Roozbehi S, Moradian C, Zahiri J, et al. Drug
1058 repositioning based on gene expression data for human HER2-positive breast cancer.
1059 Archives of Biochemistry and Biophysics. 2021;712:109043.
1060 27. Ji X, Jin C, Dong X, Dixon MS, Williams KP, Zheng W. Literature-wide association
1061 studies (LWAS) for a rare disease: drug repurposing for inflammatory breast cancer.
1062 Molecules. 2020;25(17):3933.
1063 28. Ji X, Williams KP, Zheng W. Applying a Gene Reversal Rate Computational
1064 Methodology to Identify Drugs for a Rare Cancer: Inflammatory Breast Cancer. Cancer
1065 Informatics. 2023;22:11769351231202588.
1066 29. Zheng S, Dharssi S, Wu M, Li J, Lu Z. Text mining for drug discovery.
1067 Bioinformatics and Drug Discovery. 2019:231-52.
1068 30. Jia Z, Song X, Shi J. Drug Repurposing-Molecular Aspects| Therapeutic Applications.
1069 IntechOpen; 2021.
1070 31. Chen B, Ma L, Paik H, Sirota M, Wei W, Chua M-S, et al. Reversal of cancer gene
1071 expression correlates with drug efficacy and reveals therapeutic targets. Nature
1072 communications. 2017;8(1):16022.
1073 32. Abraham VC, Towne DL, Waring JF, Warrior U, Burns DJ. Application of a high-
1074 content multiparameter cytotoxicity assay to prioritize compounds based on toxicity potential
1075 in humans. SLAS Discovery. 2008;13(6):527-37.
1076 33. Oladapo HO, Tarpley M, Sauer SJ, Addo KA, Ingram SM, Strepay D, et al.
1077 Pharmacological targeting of GLI1 inhibits proliferation, tumor emboli formation and in vivo
1078 tumor growth of inflammatory breast cancer cells. Cancer letters. 2017;411:136-49.
1079 34. Williams KP, Allensworth JL, Ingram SM, Smith GR, Aldrich AJ, Sexton JZ, et al.
1080 Quantitative high-throughput efficacy profiling of approved oncology drugs in inflammatory

1081 breast cancer models of acquired drug resistance and re-sensitization. Cancer letters.
1082 2013;337(1):77-89.
1083 35. Flobak Å, Niederdorfer B, Nakstad VT, Thommesen L, Klinkenberg G, Lægreid A. A
1084 high-throughput drug combination screen of targeted small molecule inhibitors in cancer cell
1085 lines. Scientific data. 2019;6(1):237.
1086 36. Ianevski A, Giri AK, Gautam P, Kononov A, Potdar S, Saarela J, et al. Prediction of
1087 drug combination effects with a minimal set of experiments. Nature machine intelligence.
1088 2019;1(12):568-77.
1089 37. Pemovska T, Bigenzahn JW, Superti-Furga G. Recent advances in combinatorial drug
1090 screening and synergy scoring. Current opinion in pharmacology. 2018;42:102-10.
1091 38. Ianevski A, Giri AK, Aittokallio T. SynergyFinder 3.0: an interactive analysis and
1092 consensus interpretation of multi-drug synergies across multiple samples. Nucleic acids
1093 research. 2022;50(W1):W739-W43.
1094 39. Zheng S, Wang W, Aldahdooh J, Malyutina A, Shadbahr T, Tanoli Z, et al.
1095 SynergyFinder plus: toward better interpretation and annotation of drug combination
1096 screening datasets. Genomics, Proteomics and Bioinformatics. 2022;20(3):587-96.
1097 40. Forozan F, Veldman R, Ammerman C, Parsa N, Kallioniemi A, Kallioniemi O, et al.
1098 Molecular cytogenetic analysis of 11 new breast cancer cell lines. British journal of cancer.
1099 1999;81(8):1328-34.
1100 41. Devi GR, Pai P, Lee S, Foster MW, Sannareddy DS, Bertucci F, et al. Altered
1101 ribosomal profile in acquired resistance and reversal associates with pathological response to
1102 chemotherapy in inflammatory breast cancer. NPJ Breast Cancer. 2024;10(1):65.
1103 42. Hoffmeyer MR, Wall KM, Dharmawardhane SF. In vitro analysis of the invasive
1104 phenotype of SUM 149, an inflammatory breast cancer cell line. Cancer cell international.
1105 2005;5:1-10.

1106 43. van Golen KL, Bao L, DiVito MM, Wu Z, Prendergast GC, Merajver SD. Reversion
1107 of RhoC GTPase-induced inflammatory breast cancer phenotype by treatment with a farnesyl
1108 transferase inhibitor. Molecular cancer therapeutics. 2002;1(8):575-83.
1109 44. Zeuner S, Vollmer J, Sigaud R, Oppermann S, Peterziel H, ElHarouni D, et al.
1110 Combination drug screen identifies synergistic drug interaction of BCL-XL and class I
1111 histone deacetylase inhibitors in MYC-amplified medulloblastoma cells. Journal of Neuro-
1112 oncology. 2024;166(1):99-112.
1113 45. MDAnderson. IBC Treatment Algorithm. 2023.
1114 46. Chintalaramulu N, Vadivelu R, Nguyen N-T, Cock IE. Lapatinib inhibits doxorubicin
1115 induced migration of HER2-positive breast cancer cells. Inflammopharmacology.
1116 2020;28:1375-86.
1117 47. Denkert C, Von Minckwitz G, Brase JC, Sinn BV, Gade S, Kronenwett R, et al.
1118 Tumor-infiltrating lymphocytes and response to neoadjuvant chemotherapy with or without
1119 carboplatin in human epidermal growth factor receptor 2–positive and triple-negative primary
1120 breast cancers. Journal of clinical oncology. 2015;33(9):983-91.
1121 48. Duarte D, Vale N. Evaluation of synergism in drug combinations and reference
1122 models for future orientations in oncology. Current Research in Pharmacology and Drug
1123 Discovery. 2022;3:100110.
1124 49. Malyutina A, Majumder MM, Wang W, Pessia A, Heckman CA, Tang J. Drug
1125 combination sensitivity scoring facilitates the discovery of synergistic and efficacious drug
1126 combinations in cancer. PLoS computational biology. 2019;15(5):e1006752.
1127 50. Sauer SJ, Tarpley M, Shah I, Save AV, Lyerly HK, Patierno SR, et al. Bisphenol A
1128 activates EGFR and ERK promoting proliferation, tumor spheroid formation and resistance
1129 to EGFR pathway inhibition in estrogen receptor-negative inflammatory breast cancer cells.
1130 Carcinogenesis. 2017;38(3):bgx003.

1131 51. Lederer S, Dijkstra TM, Heskes T. Additive dose response models: defining synergy.
1132 Frontiers in pharmacology. 2019;10:1384.
1133 52. Roell KR, Reif DM, Motsinger-Reif AA. An introduction to terminology and
1134 methodology of chemical synergy—perspectives from across disciplines. Frontiers in
1135 pharmacology. 2017;8:158.
1136 53. Wittman M, Carboni J, Attar R, Balasubramanian B, Balimane P, Brassil P, et al.
1137 Discovery of a 1 H-Benzoimidazol-2-yl)-1 H-pyridin-2-one (BMS-536924) inhibitor of
1138 insulin-like growth factor I receptor kinase with in vivo antitumor activity. Journal of
1139 medicinal chemistry. 2005;48(18):5639-43.
1140 54. Han Y, Caday CG, Nanda A, Cavenee WK, Huang HS. Tyrphostin AG 1478
1141 preferentially inhibits human glioma cells expressing truncated rather than wild-type
1142 epidermal growth factor receptors. Cancer research. 1996;56(17):3859-61.
1143 55. Levitzki A, Gazit A. Tyrosine kinase inhibition: an approach to drug development.
1144 Science. 1995;267(5205):1782-8.
1145 56. Kau TR, Schroeder F, Ramaswamy S, Wojciechowski CL, Zhao JJ, Roberts TM, et
1146 al. A chemical genetic screen identifies inhibitors of regulated nuclear export of a Forkhead
1147 transcription factor in PTEN-deficient tumor cells. Cancer cell. 2003;4(6):463-76.
1148 57. Hutchinson E. CCI-779: a new targeted anticancer agent. The Lancet Oncology.
1149 2000;1(4):198. doi: 10.1016/S1470-2045(00)00135-2.
1150 58. Rosenbluth JM, Overmoyer BA. Inflammatory breast cancer: a separate entity.
1151 Current Oncology Reports. 2019;21(10):86.
1152 59. Jonker AH, O'Connor D, Cavaller-Bellaubi M, Fetro C, Gogou M, 'T Hoen PA, et al.
1153 Drug repurposing for rare: progress and opportunities for the rare disease community.
1154 Frontiers in medicine. 2024;11:1352803.

1155 60. Ueno NT, Zhang D. Targeting EGFR in triple negative breast cancer. Journal of
1156 Cancer. 2011;2:324.
1157 61. Grigoriadis A, Mackay A, Noel E, Wu PJ, Natrajan R, Frankum J, et al. Molecular
1158 characterisation of cell line models for triple-negative breast cancers. BMC genomics.
1159 2012;13:1-14.
1160 62. Lacerda L, Debeb BG, Smith D, Larson R, Solley T, Xu W, et al. Mesenchymal stem
1161 cells mediate the clinical phenotype of inflammatory breast cancer in a preclinical model.
1162 Breast Cancer Research. 2015;17:1-17.
1163 63. Boussen H, Cristofanilli M, Zaks T, DeSilvio M, Salazar V, Spector N. Phase II study
1164 to evaluate the efficacy and safety of neoadjuvant lapatinib plus paclitaxel in patients with
1165 inflammatory breast cancer. Journal of clinical oncology. 2010;28(20):3248-55.
1166 64. Kaufman B, Trudeau M, Awada A, Blackwell K, Bachelot T, Salazar V, et al.
1167 Lapatinib monotherapy in patients with HER2-overexpressing relapsed or refractory
1168 inflammatory breast cancer: final results and survival of the expanded HER2+ cohort in
1169 EGF103009, a phase II study. The lancet oncology. 2009;10(6):581-8.
1170 65. Alvarez RH, Cristofanilli M, Ensor J, Lucci A, Yang WT, Le-Petross HT, et al.
1171 Limited efficacy and significant toxicities of lapatinib (Lap) plus chemotherapy as
1172 neoadjuvant therapy (NAC) for HER2-positive inflammatory breast cancer (IBC) patients
1173 (Pts). American Society of Clinical Oncology; 2012.
1174 66. Dehghan-Paz I, Il'yasova D, van Golen KL, Usha L. Tipifarnib and
1175 farnesyltransferase inhibitors in the treatment of inflammatory breast cancer: is the story
1176 over? A review. Orphan Drugs: Research and Reviews. 2013:11-21.
1177 67. Allen SG, Chen Y-C, Madden JM, Fournier CL, Altemus MA, Hiziroglu AB, et al.
1178 Macrophages enhance migration in inflammatory breast cancer cells via RhoC GTPase
1179 signaling. Scientific reports. 2016;6(1):39190.

1180 68. Fuentes-Baile M, Ventero MP, Encinar JA, García-Morales P, Poveda-Deltell M,
1181 Pérez-Valenciano E, et al. Differential effects of IGF-1R small molecule tyrosine kinase
1182 inhibitors BMS-754807 and OSI-906 on human cancer cell lines. Cancers. 2020;12(12):3717.
1183 69. Litzenburger BC, Kim H-J, Kuiatse I, Carboni JM, Attar RM, Gottardis MM, et al.
1184 BMS-536924 reverses IGF-IR-induced transformation of mammary epithelial cells and
1185 causes growth inhibition and polarization of MCF7 cells. Clinical Cancer Research.
1186 2009;15(1):226-37.
1187 70. Law JH, Habibi G, Hu K, Masoudi H, Wang MY, Stratford AL, et al. Phosphorylated
1188 insulin-like growth factor-i/insulin receptor is present in all breast cancer subtypes and is
1189 related to poor survival. Cancer research. 2008;68(24):10238-46.
1190 71. Dool CJ, Mashhedi H, Zakikhani M, David S, Zhao Y, Birman E, et al. IGF1/insulin
1191 receptor kinase inhibition by BMS-536924 is better tolerated than alloxan-induced
1192 hypoinsulinemia and more effective than metformin in the treatment of experimental insulin-
1193 responsive breast cancer. Endocrine-related cancer. 2011;18(6):699-709.
1194 72. Wang P, Mak VC, Cheung LW. Drugging IGF-1R in cancer: New insights and
1195 emerging opportunities. Genes & diseases. 2023;10(1):199-211.
1196 73. Fleming GF, Ma CX, Huo D, Sattar H, Tretiakova M, Lin L, et al. Phase II trial of
1197 temsirolimus in patients with metastatic breast cancer. Breast cancer research and treatment.
1198 2012;136:355-63.
1199 74. Baselga J, Campone M, Piccart M, Burris III HA, Rugo HS, Sahmoud T, et al.
1200 Everolimus in postmenopausal hormone-receptor–positive advanced breast cancer. New
1201 England Journal of Medicine. 2012;366(6):520-9.
1202 75. Royce ME, Osman D. Everolimus in the treatment of metastatic breast cancer. Breast
1203 cancer: basic and clinical research. 2015;9:BCBCR. S29268.

1204 76. Meinig JM, Peterson BR. Anticancer/antiviral agent Akt inhibitor-IV massively
1205 accumulates in mitochondria and potently disrupts cellular bioenergetics. ACS chemical
1206 biology. 2015;10(2):570-6.
1207 77. Chory EJ, Wang M, Ceribelli M, Michalowska AM, Golas S, Beck E, et al. High-
1208 throughput approaches to uncover synergistic drug combinations in leukemia. SLAS
1209 Discovery. 2023;28(4):193-201.
1210 78. He Y, Sun MM, Zhang GG, Yang J, Chen KS, Xu WW, et al. Targeting PI3K/Akt
1211 signal transduction for cancer therapy. Signal transduction and targeted therapy.
1212 2021;6(1):425.
1213 79. Glaviano A, Foo AS, Lam HY, Yap KC, Jacot W, Jones RH, et al. PI3K/AKT/mTOR
1214 signaling transduction pathway and targeted therapies in cancer. Molecular cancer.
1215 2023;22(1):138.
1216 80. Rascio F, Spadaccino F, Rocchetti MT, Castellano G, Stallone G, Netti GS, et al. The
1217 pathogenic role of PI3K/AKT pathway in cancer onset and drug resistance: an updated
1218 review. Cancers. 2021;13(16):3949.
1219 81. Huang F, Greer A, Hurlburt W, Han X, Hafezi R, Wittenberg GM, et al. The
1220 mechanisms of differential sensitivity to an insulin-like growth factor-1 receptor inhibitor
1221 (BMS-536924) and rationale for combining with EGFR/HER2 inhibitors. Cancer research.
1222 2009;69(1):161-70.
1223 82. Hua H, Kong Q, Yin J, Zhang J, Jiang Y. Insulin-like growth factor receptor signaling
1224 in tumorigenesis and drug resistance: a challenge for cancer therapy. Journal of hematology
1225 & oncology. 2020;13:1-17.
1226 83. Shin M, Yang EG, Song HK, Jeon H. Insulin activates EGFR by stimulating its
1227 interaction with IGF-1R in low-EGFR-expressing TNBC cells. BMB reports.
1228 2015;48(6):342.

1229 84. Haluska P, Carboni JM, TenEyck C, Attar RM, Hou X, Yu C, et al. HER receptor
1230 signaling confers resistance to the insulin-like growth factor-I receptor inhibitor, BMS-
1231 536924. Molecular cancer therapeutics. 2008;7(9):2589-98.
1232 85. Wang R, Yamada T, Kita K, Taniguchi H, Arai S, Fukuda K, et al. Transient IGF-1R
1233 inhibition combined with osimertinib eradicates AXL-low expressing EGFR mutated lung
1234 cancer. Nature communications. 2020;11(1):4607.
1235 86. Simpson A, Petnga W, Macaulay VM, Weyer-Czernilofsky U, Bogenrieder T.
1236 Insulin-like growth factor (IGF) pathway targeting in cancer: role of the IGF axis and
1237 opportunities for future combination studies. Targeted oncology. 2017;12:571-97.
1238 87. Tsai P-J, Lai Y-H, Manne RK, Tsai Y-S, Sarbassov D, Lin H-K. Akt: a key
1239 transducer in cancer. Journal of biomedical science. 2022;29(1):76.
1240 88. Memmott RM, Dennis PA. Akt-dependent and-independent mechanisms of mTOR
1241 regulation in cancer. Cellular signalling. 2009;21(5):656-64.
1242 89. Panwar V, Singh A, Bhatt M, Tonk RK, Azizov S, Raza AS, et al. Multifaceted role
1243 of mTOR (mammalian target of rapamycin) signaling pathway in human health and disease.
1244 Signal transduction and targeted therapy. 2023;8(1):375.
1245 90. Zhang H, Berel D, Wang Y, Li P, Bhowmick NA, Figlin RA, et al. A comparison of
1246 Ku0063794, a dual mTORC1 and mTORC2 inhibitor, and temsirolimus in preclinical renal
1247 cell carcinoma models. PloS one. 2013;8(1):e54918.
1248 91. Pervanidis KA, D'Angelo GD, Weisner J, Brandherm S, Rauh D. Akt inhibitor
1249 advancements: from capivasertib approval to covalent-allosteric promises. Journal of
1250 medicinal chemistry. 2024;67(8):6052-63.
1251 92. Shirley M. Capivasertib: first approval. Drugs. 2024;84(3):337-46.
1252 93. Ahmad S, He Q, Williams KP, Scott JE. Identification of a triple drug combination
1253 that is synergistically cytotoxic for triple-negative breast cancer cells using a novel

1254 combination discovery approach. SLAS DISCOVERY: Advancing the Science of Drug
1255 Discovery. 2020;25(8):923-38.
1256 94. Barbone D, Yang T-M, Morgan JR, Gaudino G, Broaddus VC. Mammalian target of
1257 rapamycin contributes to the acquired apoptotic resistance of human mesothelioma
1258 multicellular spheroids. Journal of Biological Chemistry. 2008;283(19):13021-30.
1259 95. Lehman HL, Van Laere SJ, van Golen CM, Vermeulen PB, Dirix LY, van Golen KL.
1260 Regulation of inflammatory breast cancer cell invasion through Akt1/PKBα phosphorylation
1261 of RhoC GTPase. Molecular Cancer Research. 2012;10(10):1306-18.
1262 96. Zhang D, LaFortune TA, Krishnamurthy S, Esteva FJ, Cristofanilli M, Liu P, et al.
1263 Epidermal growth factor receptor tyrosine kinase inhibitor reverses mesenchymal to
1264 epithelial phenotype and inhibits metastasis in inflammatory breast cancer. Clinical Cancer
1265 Research. 2009;15(21):6639-48.
1266 97. Gohr K, Hamacher A, Engelke LH, Kassack MU. Inhibition of PI3K/Akt/mTOR
1267 overcomes cisplatin resistance in the triple negative breast cancer cell line HCC38. BMC
1268 cancer. 2017;17:1-13.
1269 98. Acevedo-Díaz A, Morales-Cabán BM, Zayas-Santiago A, Martínez-Montemayor
1270 MM, Suárez-Arroyo IJ. SCAMP3 regulates EGFR and promotes proliferation and migration
1271 of triple-negative breast cancer cells through the modulation of AKT, ERK, and STAT3
1272 signaling pathways. Cancers. 2022;14(11):2807.
1273 99. Chin YR, Toker A. The actin-bundling protein palladin is an Akt1-specific substrate
1274 that regulates breast cancer cell migration. Molecular cell. 2010;38(3):333-44.
1275 100. Morrison Joly M, Williams MM, Hicks DJ, Jones B, Sanchez V, Young CD, et al.
1276 Two distinct mTORC2-dependent pathways converge on Rac1 to drive breast cancer
1277 metastasis. Breast Cancer Research. 2017;19:1-15.

1278 101. Soni UK, Jenny L, Hegde RS. IGF-1R targeting in cancer–does sub-cellular
1279 localization matter? Journal of Experimental & Clinical Cancer Research. 2023;42(1):273.
1280 102. O'Reilly KE, Rojo F, She Q-B, Solit D, Mills GB, Smith D, et al. mTOR inhibition
1281 induces upstream receptor tyrosine kinase signaling and activates Akt. Cancer research.
1282 2006;66(3):1500-8.
1283 103. Abdel-Rahman MA, Mahfouz M, Habashy HO. RRM2 expression in different
1284 molecular subtypes of breast cancer and its prognostic significance. Diagnostic pathology.
1285 2022;17(1):1.
1286 104. Zuo Z, Zhou Z, Chang Y, Liu Y, Shen Y, Li Q, et al. Ribonucleotide reductase M2
1287 (RRM2): Regulation, function and targeting strategy in human cancer. Genes & diseases.
1288 2024;11(1):218-33.
1289 105. Milioli H, Alexandrou S, Lim E, Caldon CE. Cyclin E1 and cyclin E2 in ER+ breast
1290 cancer: prospects as biomarkers and therapeutic targets. Endocrine-related cancer.
1291 2020;27(5):R93-R112.
1292 106. Alexander A, Karakas C, Chen X, Carey JP, Yi M, Bondy M, et al. Cyclin E
1293 overexpression as a biomarker for combination treatment strategies in inflammatory breast
1294 cancer. Oncotarget. 2017;8(9):14897.

1295

1296 Supporting information

1297 Supplemental Figure Legends

1298 **S1 Fig. Representative dose response curves for the LWAS drug candidates with efficacy**
1299 **in breast cancer cell lines using the Hoechst assay.** (A) SUM159, (B) MDA-MB-231, and
1300 (C) MCF-7. Each graph shows the relative cell count (%) plotted against drug concentration

1301 (μM) on a logarithmic scale. Plots are grouped by drug mechanisms: antimetabolites,
1302 microtubule inhibitors, topoisomerase inhibitors, and tyrosine kinase Inhibitors. Error bars
1303 indicate ± SD from replicate experiments.

1304

1305 **S2 Fig. Representative dose response curves of the GRR effective compounds with**
1306 **efficacy in different breast cancer cell lines using the Hoechst assay.** (A) SUM159, (B)
1307 MDA-MB-231 and (C) MCF-7s. The x axis represents the concentration of the compound in
1308 μM while the y axis represents the cell count % normalized to DMSO control. All the
1309 experiments were done in technical and independent experiments (n=3). Error bars indicate ±
1310 SD from replicate experiments.

1311

1312 **S3 Fig. Drug sensitivity heatmap profiles and dose response curves for LWAS drugs in**
1313 **IBC and non-IBC breast cancer cell line panel by MTT assay.** (A) Drug response heatmaps
1314 across all the breast cancer cell lines. The x-axis represents the concentration of each drug
1315 delivered in a dose-response, while the y-axis lists the compounds. The color gradient indicates
1316 the level of inhibition, with red indicating higher inhibition and green indicating lower
1317 inhibition. Representative dose response curves grouped by drug class: antimetabolites,
1318 microtubule inhibitors, topoisomerase inhibitors, and tyrosine kinase inhibitors (TKIs), for (B)
1319 SUM149, (C) SUM159, (D) MDA-MB-231 and (E) MCF-7. Inhibition data plotted as the
1320 percentage (%) of cell proliferation relative to control versus drug concentration (μM). Error
1321 bars indicate ± SD from replicate experiments.

1322

1323 **S4 Fig**. **Drug sensitivity heatmap profiles and dose response curves for GRR drugs in IBC**
1324 **and non-IBC breast cancer cell line panel by MTT assay.** (A) Drug response heatmaps
1325 across all the breast cancer cell lines. The x-axis represents the concentration of each drug
1326 delivered in a dose-response, while the y-axis lists the compounds. The color gradient indicates
1327 the level of inhibition, with red indicating higher inhibition and green indicating lower
1328 inhibition. Representative dose response curves for each drug: BMS-536924, BMS-754807,
1329 Akt Inhibitor IV, temsirolimus, tipifranib, and tyrphostin AG 1478 in the four breast cancer
1330 cell lines with (B) SUM149, (C) SUM159, (D) MDA-MB-231 and (E) MCF-7. Inhibition data
1331 plotted as the percentage (%) of cell proliferation relative to control versus drug concentration
1332 (μM). Error bars indicate ± SD from replicate experiments.

1333

1334 **S5 Fig**. **Contour Plots of selected LWAS drug combinations with their synergy scores**
1335 **across Bliss, ZIP, Loewe and HSA reference models obtained from SynergyFinder3.**
1336 Synergy scores across Bliss, ZIP, Loewe and HSA reference models were obtained from
1337 SynergyFinder3. (A) Lapatinib + doxorubicin (B) Lapatinib + carboplatin (C) Carboplatin +
1338 etoposide (D) Carboplatin + topotecan (E) Vincristine + docetaxel, (F) Gefitinib + carboplatin
1339 and (G) Carboplatin + cytarabine. In each plot, x and y axes represent drug concentrations
1340 (μM). Red areas indicate synergy, while green areas indicate antagonism. Black boxes
1341 highlight the MSA, with scores shown. Red circles in the top right corner of each plot indicate
1342 the overall δ score. Color scales on the right of each plot show the range of synergy scores. The
1343 data represented the average of three independent experiments (n = 3).

1344

1345 **S6 Fig. Quantitative synergy analysis of GRR drug combinations in SUM149 2D and 3D**
1346 **SUM149 cell models.** Synergy scores were computed using SynergyFinder+ across four

1347 established reference models (ZIP, HSA, Bliss, and Loewe). Results are shown as bar plots for
1348 each combination. (**A**) BMS-536924 and Tyrphostin AG-1478 combination, (**B**) BMS-536924
1349 and Akt Inhibitor IV combination, and (**C**) Temsirolimus and Akt Inhibitor IV combination.
1350 The upper figure for each combination represents the results from the 2D experiments, while
1351 the lower figure represents the results from the 3D experiments. Bar plots represent the drug
1352 combination landscape, where red bars indicate positive synergy scores, and green bars indicate
1353 antagonistic effects. Blue bars highlight the optimal combinations achieving maximal synergy
1354 scores and growth inhibition while minimizing individual drug concentration, which were: (1
1355 μM BMS-536924 + 0.1 μM tyrphostin AG-1478), (1 μM BMS-536924 + 1 μM Akt Inhibitor
1356 IV), and (10 μM temsirolimus + 0.1 μM Akt Inhibitor IV). The data shown represents the
1357 average of three independent experiments.

1358

1359 **S7 Fig. Western blot analysis of protein expression levels in response to the selected GRR**
1360 **drugs and combinations.** Representative whole-blot Western blots for replicate DMSO and
1361 combination incubations with SUM149 cells. (A) Temsirolimus (10 μM) and Akt inhibitor IV
1362 (0.1 μM) combination effects on the expression of p-Akt, total Akt, p-mTOR, and total mTOR;
1363 (B) Akt Inhibitor IV (1 μM) and BMS-536924 (1 μM) combination effects on the expression
1364 of p-Akt, total Akt, p-IGF1-R, and total IGF1-R; and (C) Tyrphostin AG-1478 (0.1 μM) and
1365 BMS-536924 (1 μM) combination effects on the expression of p-EGFR, total EGFR, p-IGF1-
1366 R, and total IGF1-R. β-actin served as a loading control. Right panels show densitometric band
1367 quantification of DMSO relative to each treatment. The Li-COR system was used for all
1368 proteins except for IGF1-R and pIGF1-R, for which we used HRP-tagged secondary antibodies
1369 and iBRIGHT imaging. Statistical significance set as *P < 0.05, **P < 0.01, ***P < 0.001.

1370

1371 **S8 Fig. Global gene expression changes induced by GRR combinations in SUM149 cells.**
1372 SUM149 cells were incubated with GRR combinations or DMSO alone for 24 h, and RNA
1373 isolated for RNA-Seq (n = 3 biological replicates). RNA-Seq data were analyzed to identify
1374 genes significantly differentially expressed in SUM149 cells (padj < 0.05). (A) Differential
1375 gene expression (DGE) analysis. The number of genes differentially expressed in the
1376 combination treatment relative to the DMSO control. Total (black columns), up-regulated (red
1377 columns) and down-regulated (blue columns). (B) Volcano plots display log2 fold change
1378 (x-axis) versus −log10 p value (y-axis); vertical red lines mark the fold-change cutoffs, and the
1379 horizontal line denotes the significance threshold (FDR-adjusted $p < 0.05$). Red points indicate
1380 upregulated transcripts, and blue points indicate downregulated transcripts; representative top
1381 hits are labeled. (C) Heat maps show normalized expression values (log scale; blue = lower,
1382 red = higher) for the top 25 up-regulated and top 25 down-regulated protein-coding genes
1383 across biological triplicates. (i) to (iii) Treatment comparison: (i) DMSO (0.2%) vs
1384 BMS-536924 (1 μM) + tyrphostin AG1478 (0.1 μM) (BMS24-Tyrpho). (ii) DMSO (0.2%) vs
1385 BMS-536924 (1 μM) + AKTIV (1 μM) (BMS24-Akt). (iii) DMSO (0.2%) vs AKTIV (0.1 μM)
1386 + temsirolimus (10 μM) (Tem-Akt).
1387 Compared with DMSO, the BMS-536924 + tyrphostin AG1478 group showed the
1388 strongest transcriptional response, with 2868 DEGs, followed by AKTIV + temsirolimus with
1389 2434 DEGs. Together, these results show that each combination affects the cells differently,
1390 with BMS-536924 + tyrphostin AG1478 having the greatest overall impact. Heatmap analysis
1391 revealed that this combination induced significant changes in genes such as GSTA2, OMD,
1392 and HIST1H2AJ. Volcano plots further highlight important gene shifts, including decreases in
1393 F3, UHRF1, and RRM2, and increases in PDK4, MMP7, and ELF3, confirming the substantial
1394 impact of the BMS-536924 + tyrphostin AG1478 combination.
1395

1396 # Supplemental Tables

1397 **S1 Table. The 24 LWAS identified drugs for IBC (from Ji et al., 2020).** The table presents
1398 the corresponding drug class, PubMed entry, Clinical Trials entry, and NCT number.

1399 **S2 Table. The 19 GRR identified drugs/compounds (from Ji et al., 2023)**. The table shows
1400 with the corresponding drug class for each drug and its mechanism of action.

1401 **S3 Table. Efficacy of LWAS and GRR predicted drugs and compounds in four breast**
1402 **cancer cell lines using the MTT assay.** The table lists the IC_{50} values for each drug determined
1403 in the MTT assay across the cell lines, with values reported as the mean ± SD from 2
1404 independent experiments.

1405 **S4 Table. Selected drugs and compounds from LWAS and GRR active lists for**
1406 **combination studies.** The table shows their corresponding EC_{25} values and the highest
1407 concentration used for the 8 x 8 matrix.

1408

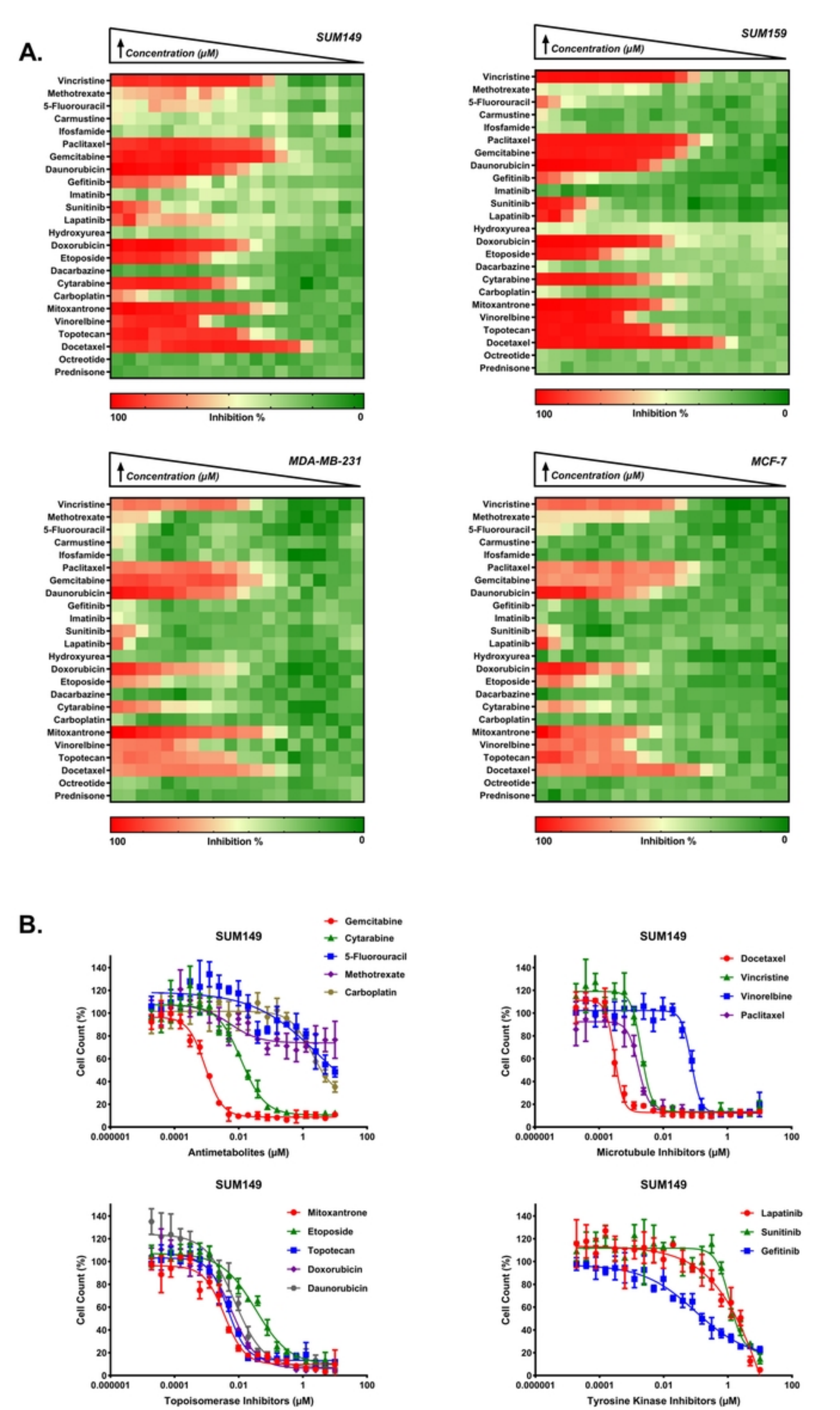
A.
SUM149
SUM159
MDA-MB-231
MCF-7
Concentration (μM)
Vincristine
Methotrexate
5-Fluorouracil
Carmustine
Ifosfamide
Paclitaxel
Gemcitabine
Daunorubicin
Gefitinib
Imatinib
Sunitinib
Lapatinib
Hydroxyurea
Doxorubicin
Etoposide
Dacarbazine
Cytarabine
Carboplatin
Mitoxantrone
Vinorelbine
Topotecan
Docetaxel
Octreotide
Prednisone
100
Inhibition %
0
B.
SUM149
Gemcitabine
Cytarabine
5-Fluorouracil
Methotrexate
Carboplatin
Cell Count (%)
Antimetabolites (μM)
Docetaxel
Vincristine
Vinorelbine
Paclitaxel
Microtubule Inhibitors (μM)
Mitoxantrone
Etoposide
Topotecan
Doxorubicin
Daunorubicin
Topoisomerase Inhibitors (μM)
Lapatinib
Sunitinib
Gefitinib
Tyrosine Kinase Inhibitors (μM)
0.000001
0.0001
0.01
1
100

Figure 1

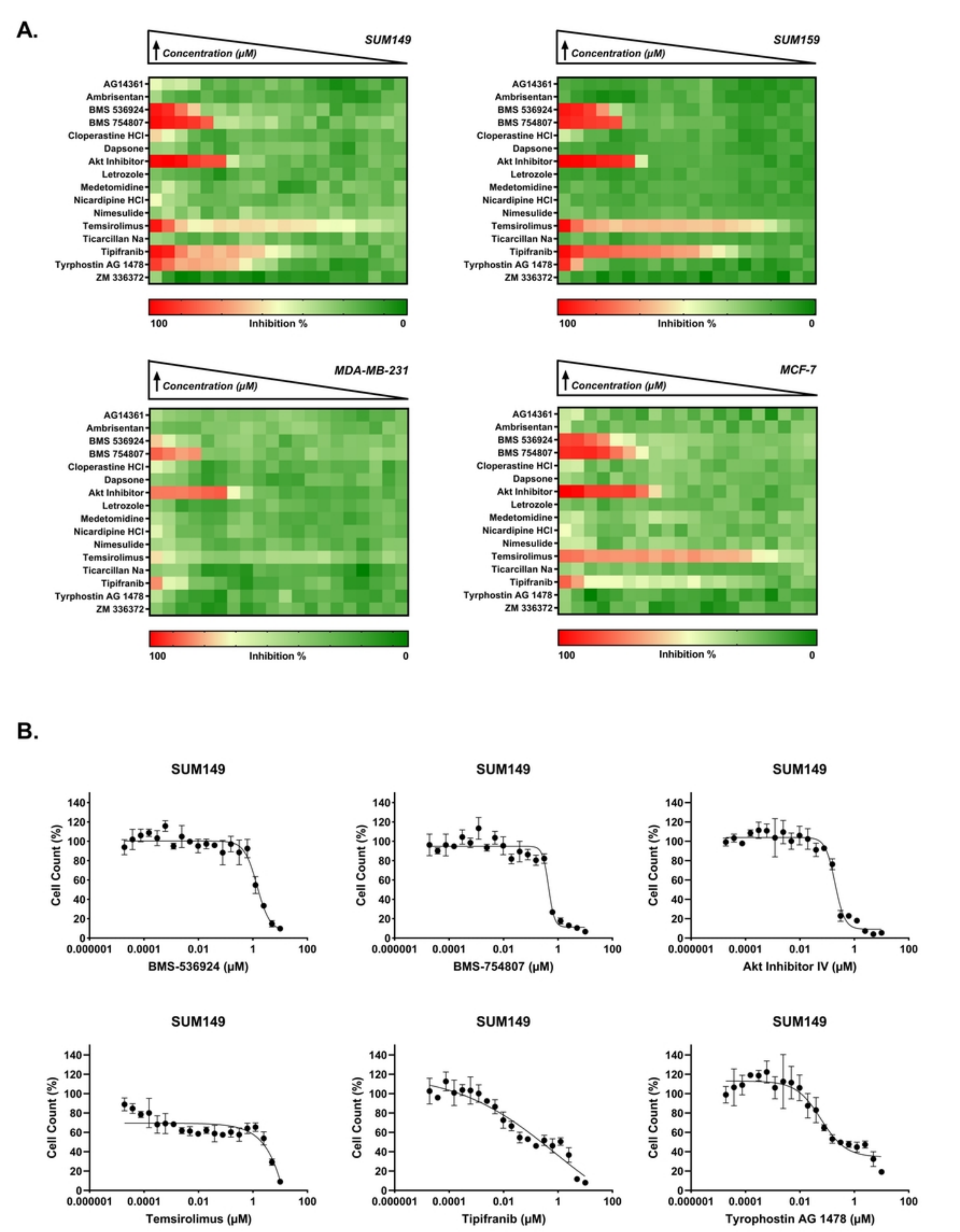
A.
SUM149
SUM159
MDA-MB-231
MCF-7
Concentration (μM)
AG14361
Ambrisentan
BMS 536924
BMS 754807
Cloperastine HCl
Dapsone
Akt Inhibitor
Letrozole
Medetomidine
Nicardipine HCl
Nimesulide
Temsirolimus
Ticarcillan Na
Tipifranib
Tyrphostin AG 1478
ZM 336372
100
Inhibition %
0
B.
SUM149
Cell Count (%)
BMS-536924 (μM)
BMS-754807 (μM)
Akt Inhibitor IV (μM)
Temsirolimus (μM)
Tipifranib (μM)
Tyrophostin AG 1478 (μM)
0.000001
0.0001
0.01
1
100

Figure 2

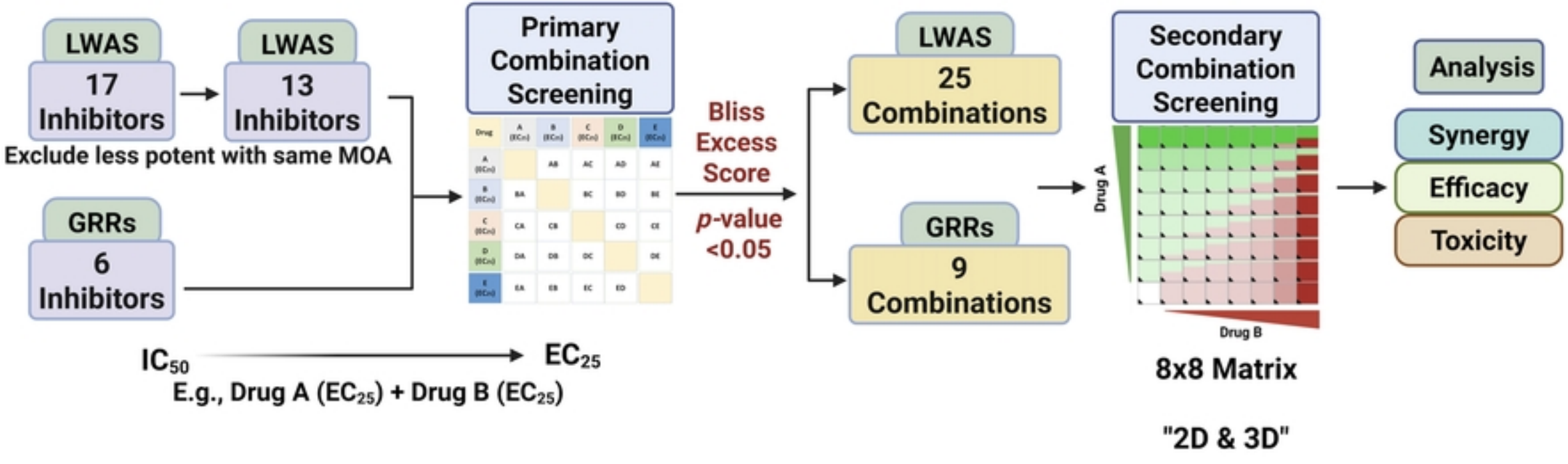
LWAS
17 Inhibitors
LWAS
13 Inhibitors
Exclude less potent with same MOA
GRRs
6 Inhibitors
Primary Combination Screening
Bliss Excess Score
p-value <0.05
LWAS
25 Combinations
GRRs
9 Combinations
Secondary Combination Screening
Drug A
Drug B
8x8 Matrix
"2D & 3D"
Analysis
Synergy
Efficacy
Toxicity
IC50
EC25
E.g., Drug A (EC25) + Drug B (EC25)

Figure 3

A.

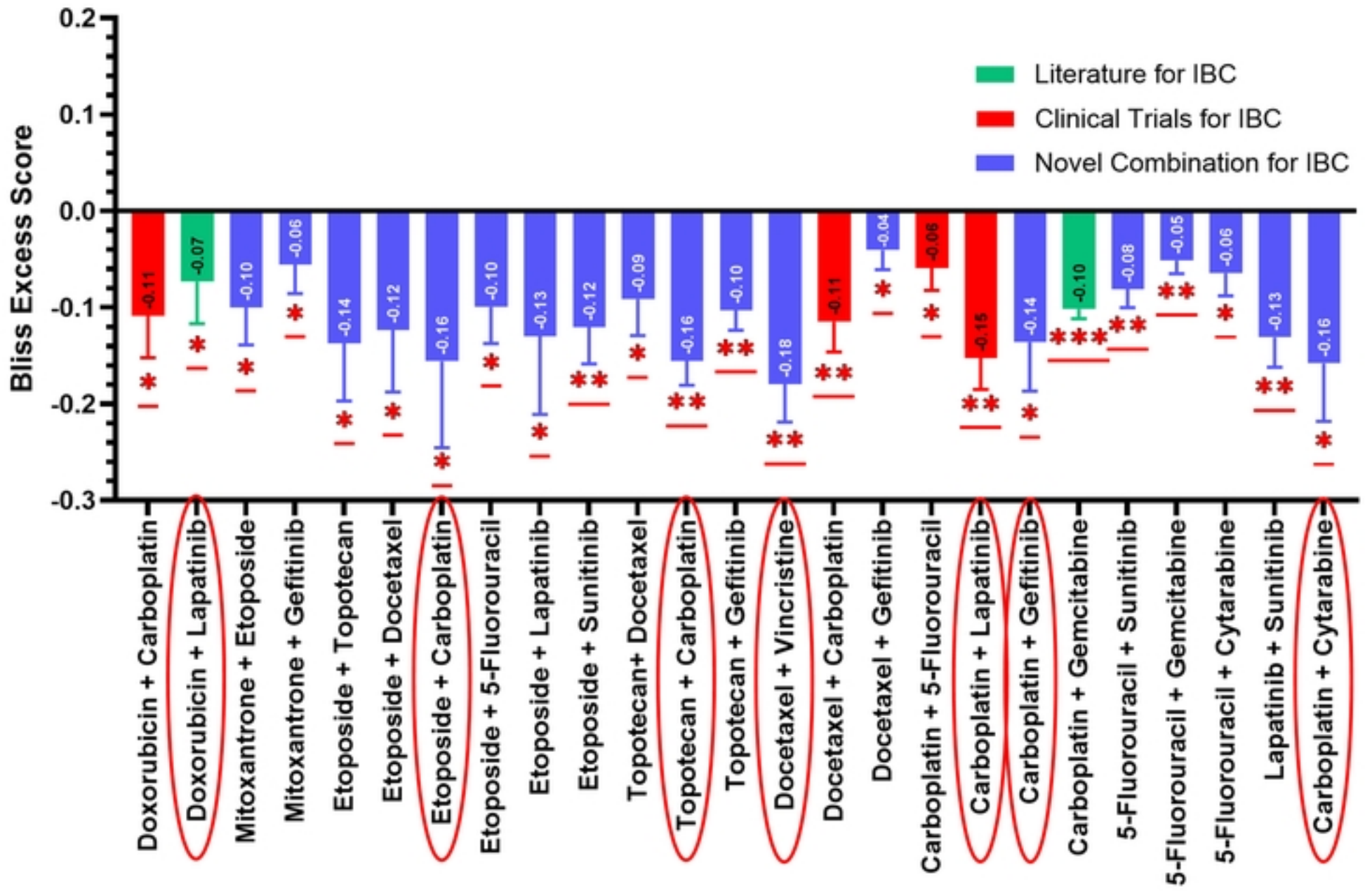
LWAS
Bliss Excess Score
0.2
0.1
0.0
-0.1
-0.2
-0.3
Literature for IBC
Clinical Trials for IBC
Novel Combination for IBC
-0.11
-0.07
-0.10
-0.06
-0.14
-0.12
-0.16
-0.10
-0.13
-0.12
-0.09
-0.16
-0.10
-0.18
-0.11
-0.04
-0.06
-0.15
-0.14
-0.10
-0.08
-0.05
-0.06
-0.13
-0.16
Doxorubicin + Carboplatin
Doxorubicin + Lapatinib
Mitoxantrone + Etoposide
Mitoxantrone + Gefitinib
Etoposide + Topotecan
Etoposide + Docetaxel
Etoposide + Carboplatin
Etoposide + 5-Fluorouracil
Etoposide + Lapatinib
Etoposide + Sunitinib
Topotecan+ Docetaxel
Topotecan + Carboplatin
Topotecan + Gefitinib
Docetaxel + Vincristine
Docetaxel + Carboplatin
Docetaxel + Gefitinib
Carboplatin + 5-Fluorouracil
Carboplatin + Lapatinib
Carboplatin + Gefitinib
Carboplatin + Gemcitabine
5-Fluorouracil + Sunitinib
5-Fluorouracil + Gemcitabine
5-Fluorouracil + Cytarabine
Lapatinib + Sunitinib
Carboplatin + Cytarabine

B.

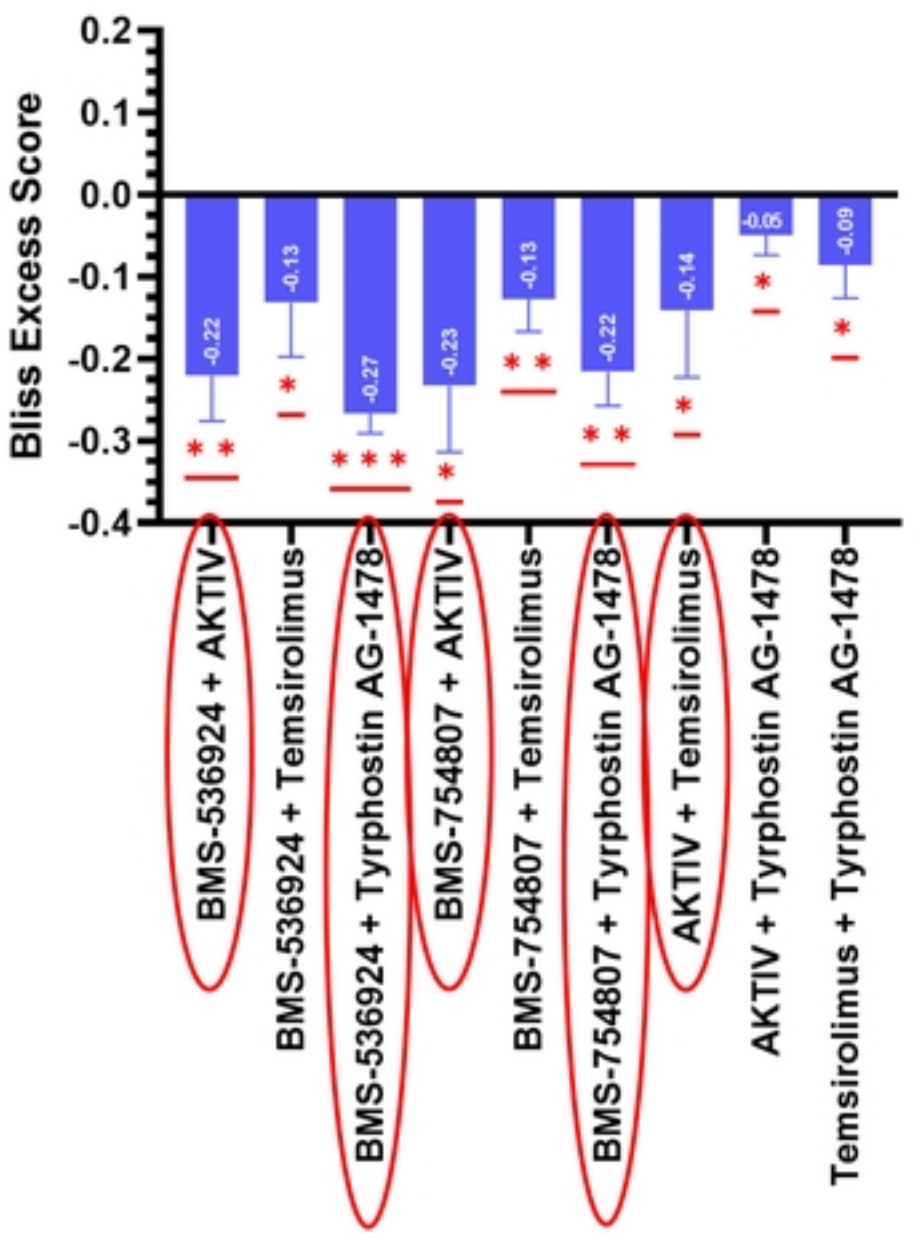
GRR
Bliss Excess Score
0.2
0.1
0.0
-0.1
-0.2
-0.3
-0.4
-0.22
-0.13
-0.27
-0.23
-0.13
-0.22
-0.14
-0.06
-0.09
BMS-536924 + AKTIV
BMS-536924 + Temsirolimus
BMS-536924 + Tyrphostin AG-1478
BMS-754807 + AKTIV
BMS-754807 + Temsirolimus
BMS-754807 + Tyrphostin AG-1478
AKTIV + Temsirolimus
AKTIV + Tyrphostin AG-1478
Temsirolimus + Tyrphostin AG-1478

Figure 4

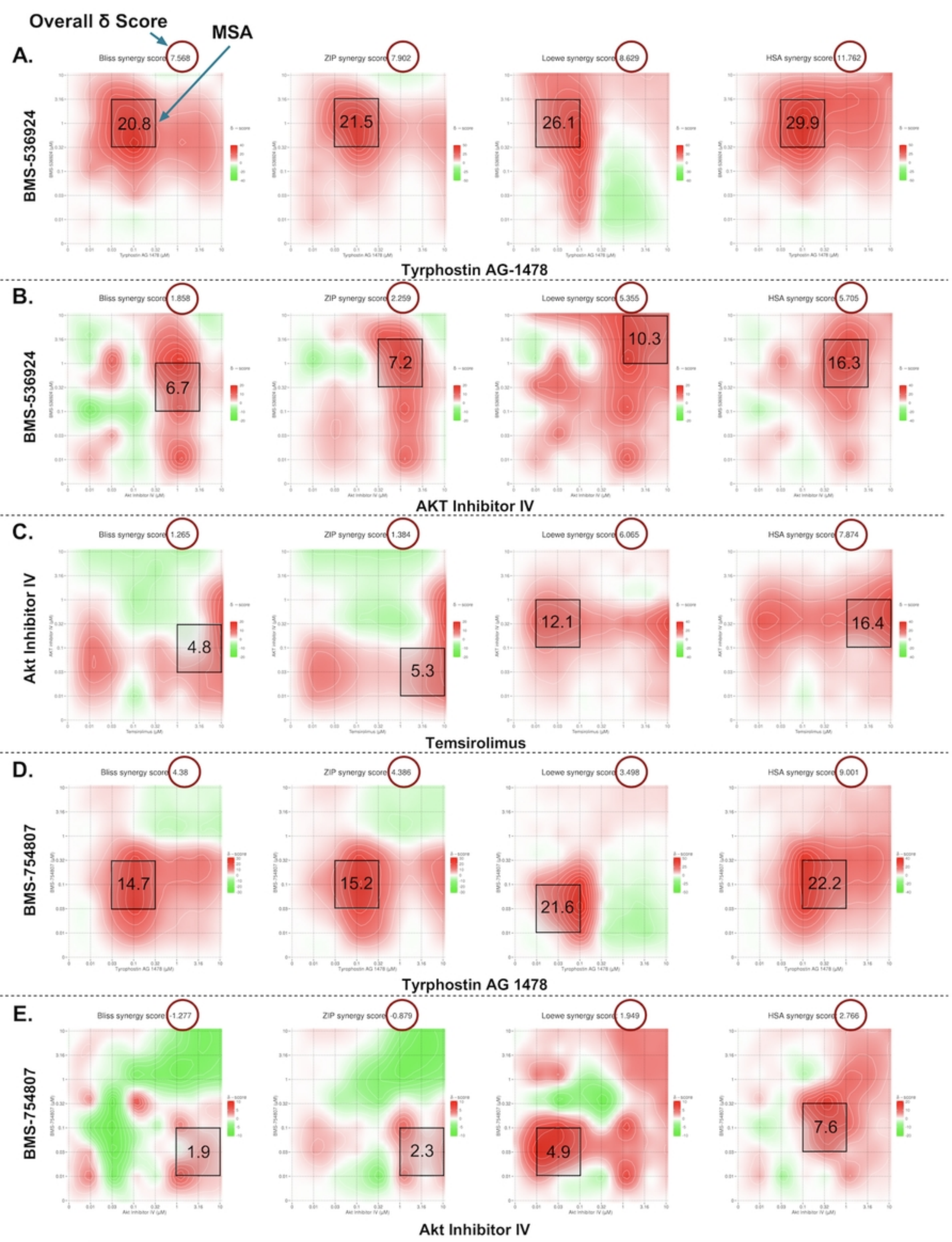
Overall δ Score
MSA
A.
Bliss synergy score 7.568
ZIP synergy score 7.902
Loewe synergy score 8.629
HSA synergy score 11.762
20.8
21.5
26.1
29.9
BMS-536924
Tyrphostin AG-1478
B.
Bliss synergy score 1.858
ZIP synergy score 2.259
Loewe synergy score 5.355
HSA synergy score 5.705
6.7
7.2
10.3
16.3
BMS-536924
AKT Inhibitor IV
C.
Bliss synergy score 1.265
ZIP synergy score 1.384
Loewe synergy score 6.065
HSA synergy score 7.874
4.8
5.3
12.1
16.4
Akt Inhibitor IV
Temsirolimus
D.
Bliss synergy score 4.38
ZIP synergy score 4.386
Loewe synergy score 3.498
HSA synergy score 9.001
14.7
15.2
21.6
22.2
BMS-754807
Tyrphostin AG 1478
E.
Bliss synergy score -1.277
ZIP synergy score -0.879
Loewe synergy score 1.949
HSA synergy score 2.766
1.9
2.3
4.9
7.6
BMS-754807
Akt Inhibitor IV

Figure 5

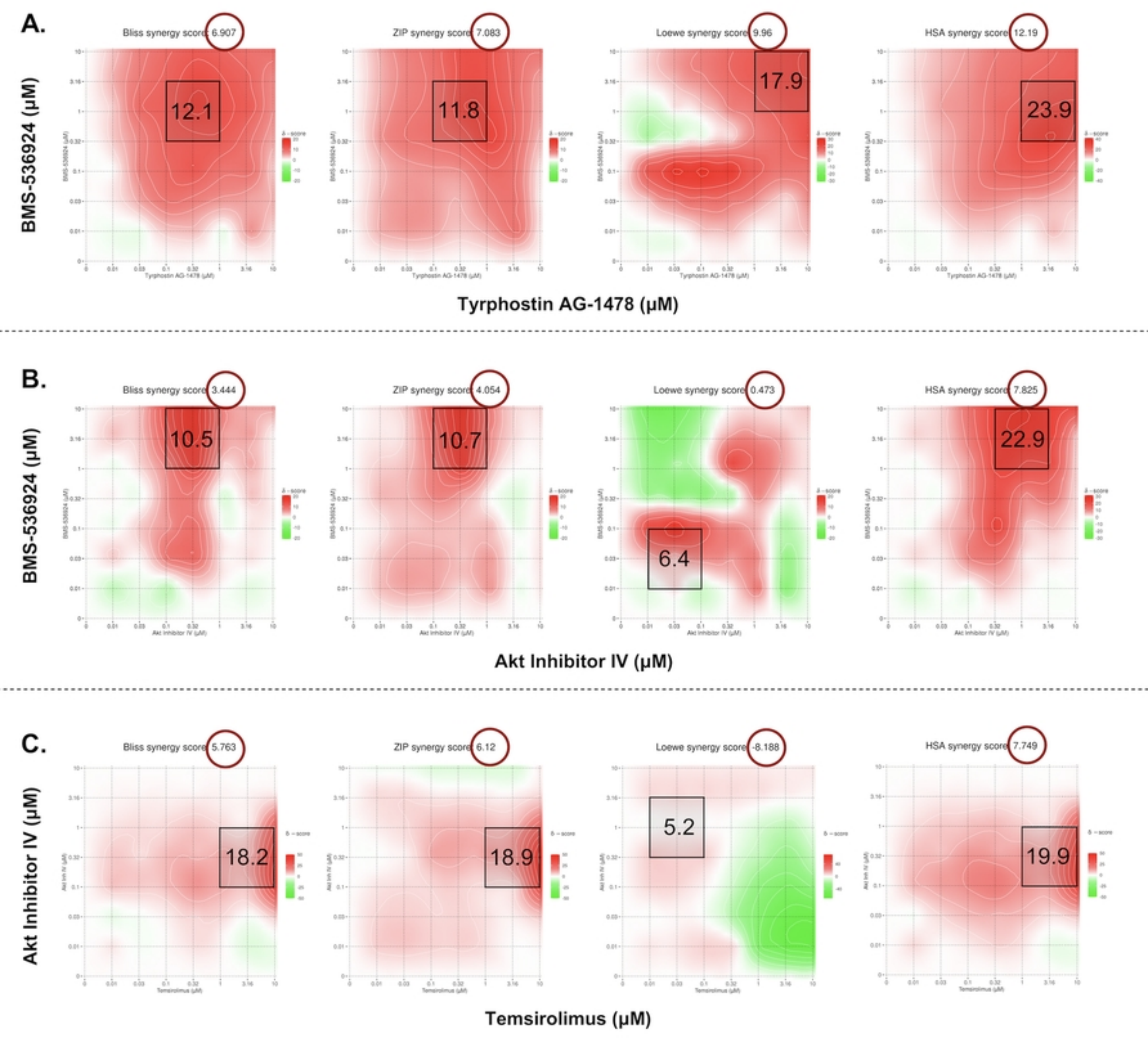
A.
Bliss synergy score 6.907
12.1
ZIP synergy score 7.083
11.8
Loewe synergy score 9.96
17.9
HSA synergy score 12.19
23.9
BMS-536924 (μM)
Tyrphostin AG-1478 (μM)
B.
Bliss synergy score 3.444
10.5
ZIP synergy score 4.054
10.7
Loewe synergy score 0.473
6.4
HSA synergy score 7.825
22.9
BMS-536924 (μM)
Akt Inhibitor IV (μM)
C.
Bliss synergy score 5.763
18.2
ZIP synergy score 6.12
18.9
Loewe synergy score -8.188
5.2
HSA synergy score 7.749
19.9
Akt Inhibitor IV (μM)
Temsirolimus (μM)

Figure 6

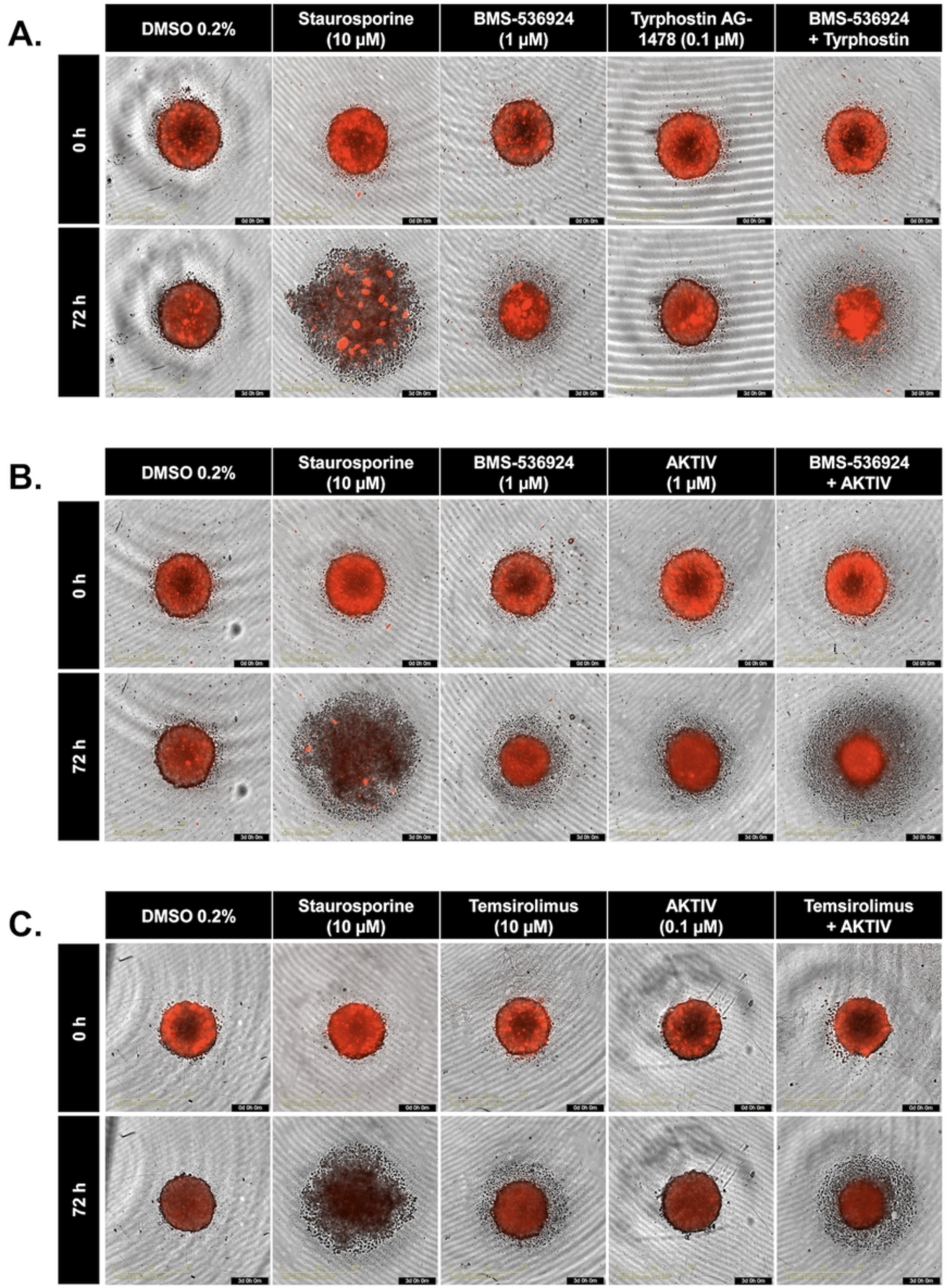
A.
DMSO 0.2%
Staurosporine (10 µM)
BMS-536924 (1 µM)
Tyrphostin AG-1478 (0.1 µM)
BMS-536924 + Tyrphostin
0 h
72 h
B.
DMSO 0.2%
Staurosporine (10 µM)
BMS-536924 (1 µM)
AKTIV (1 µM)
BMS-536924 + AKTIV
0 h
72 h
C.
DMSO 0.2%
Staurosporine (10 µM)
Temsirolimus (10 µM)
AKTIV (0.1 µM)
Temsirolimus + AKTIV
0 h
72 h

Figure 7

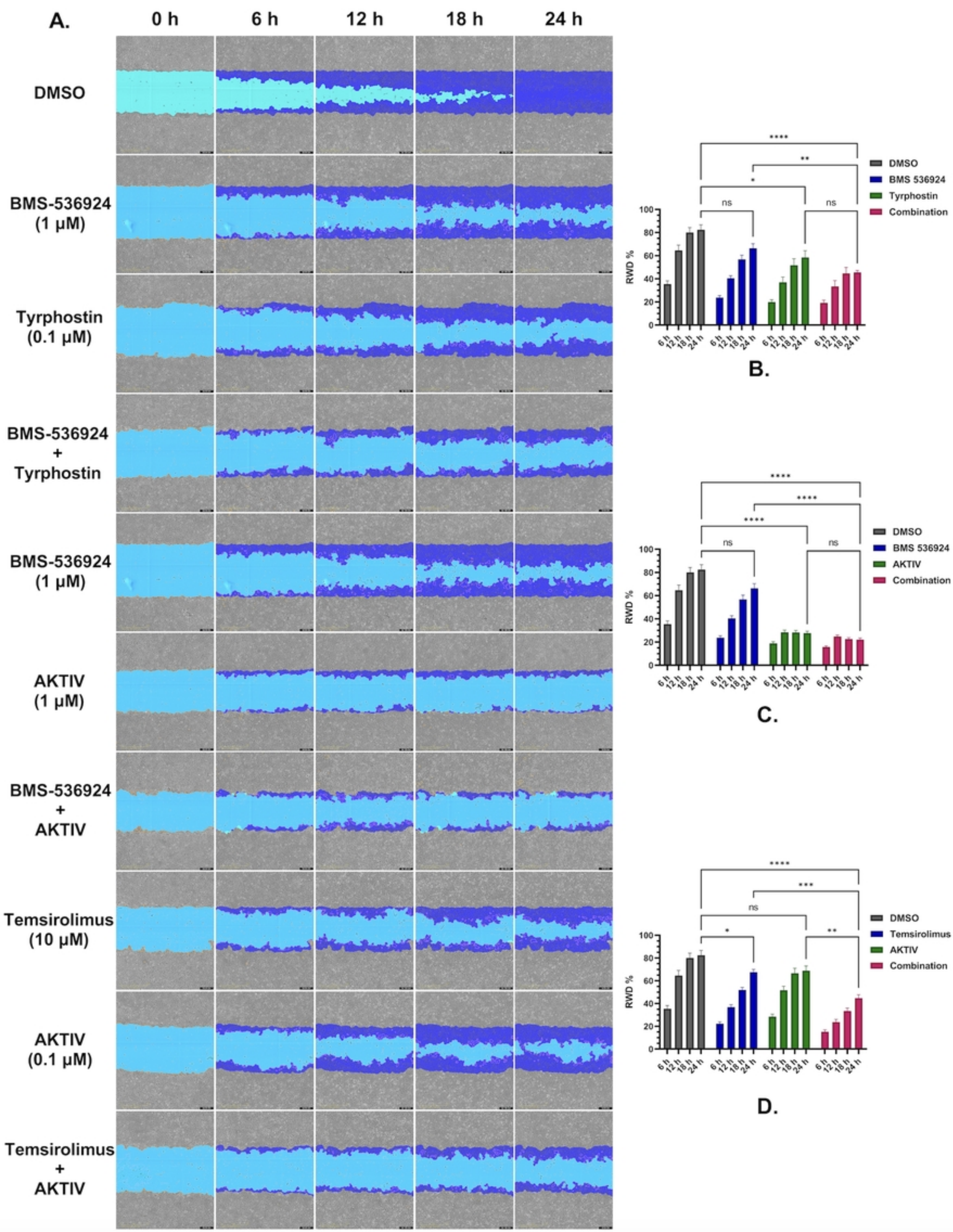
A.
0 h
6 h
12 h
18 h
24 h
DMSO
BMS-536924 (1 µM)
Tyrphostin (0.1 µM)
BMS-536924 + Tyrphostin
BMS-536924 (1 µM)
AKTIV (1 µM)
BMS-536924 + AKTIV
Temsirolimus (10 µM)
AKTIV (0.1 µM)
Temsirolimus + AKTIV
B.
RWD %
DMSO
BMS 536924
Tyrphostin
Combination
C.
AKTIV
D.
Temsirolimus

Figure 8

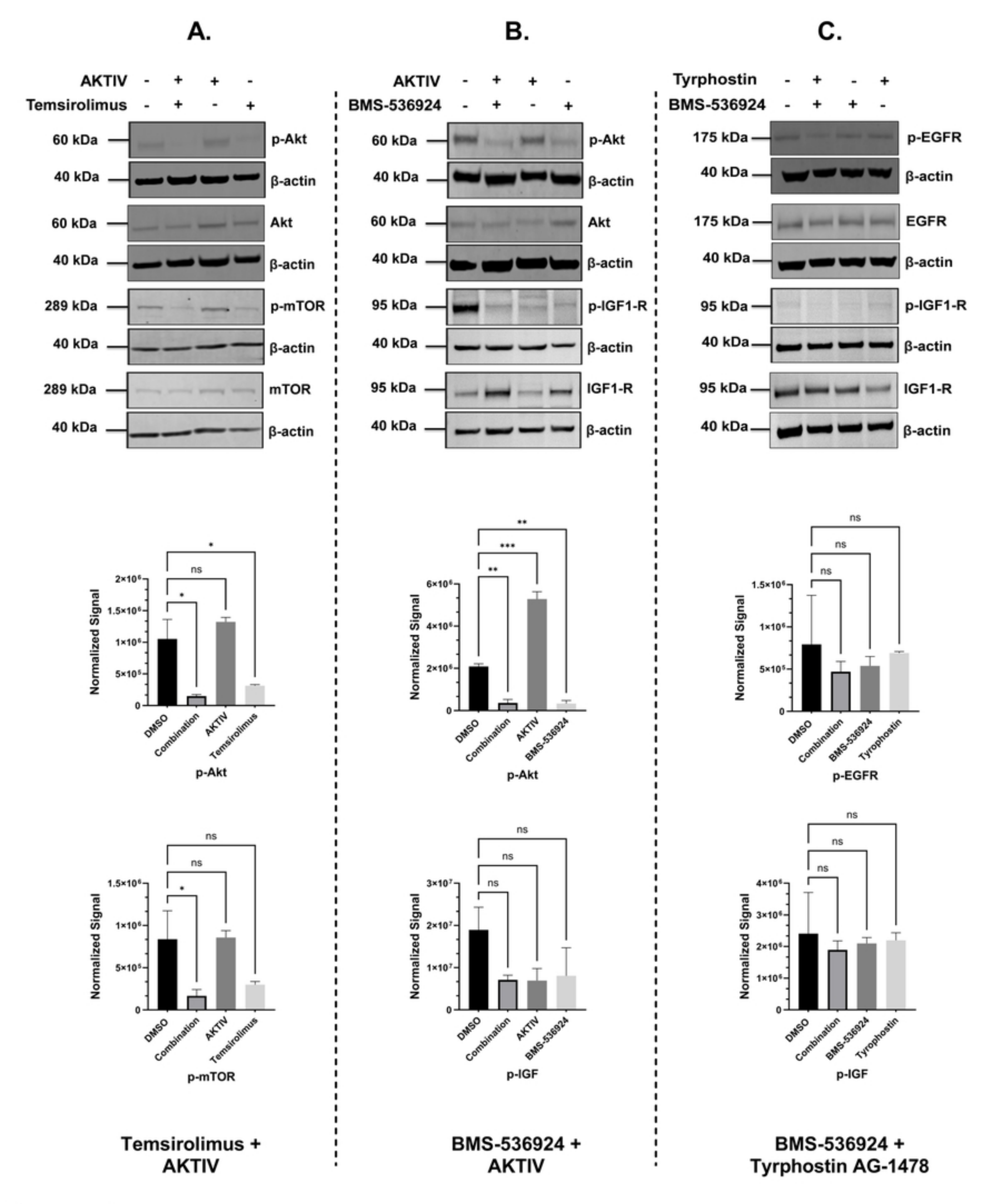
A.
B.
C.
AKTIV
Temsirolimus
BMS-536924
Tyrphostin
60 kDa
40 kDa
289 kDa
95 kDa
175 kDa
p-Akt
β-actin
Akt
p-mTOR
mTOR
p-IGF1-R
IGF1-R
p-EGFR
EGFR
Normalized Signal
DMSO
Combination
Temsirolimus
p-mTOR
p-IGF
p-EGFR
Temsirolimus + AKTIV
BMS-536924 + AKTIV
BMS-536924 + Tyrphostin AG-1478

Figure 9

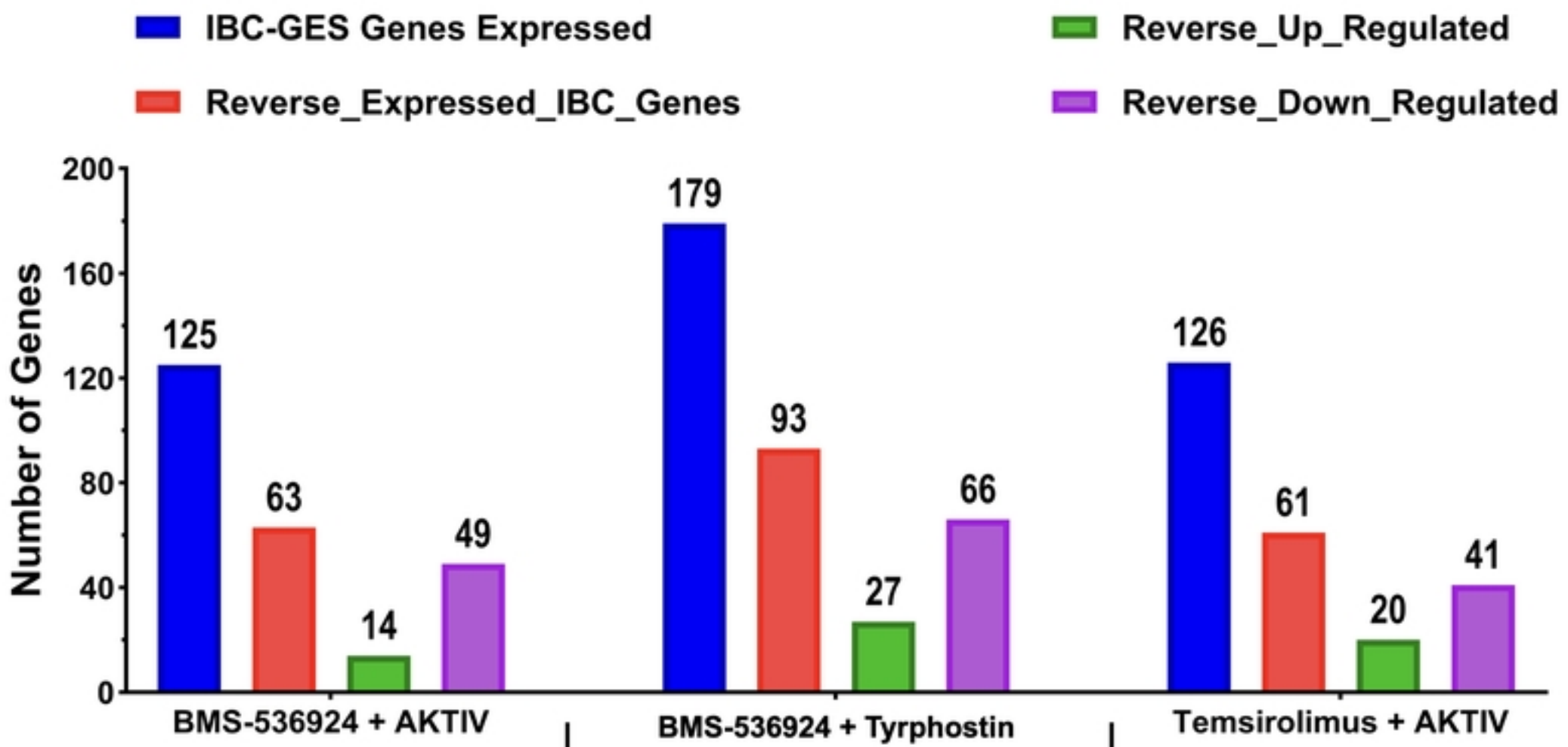

GRR Score (%)	50	52	48

Figure 10

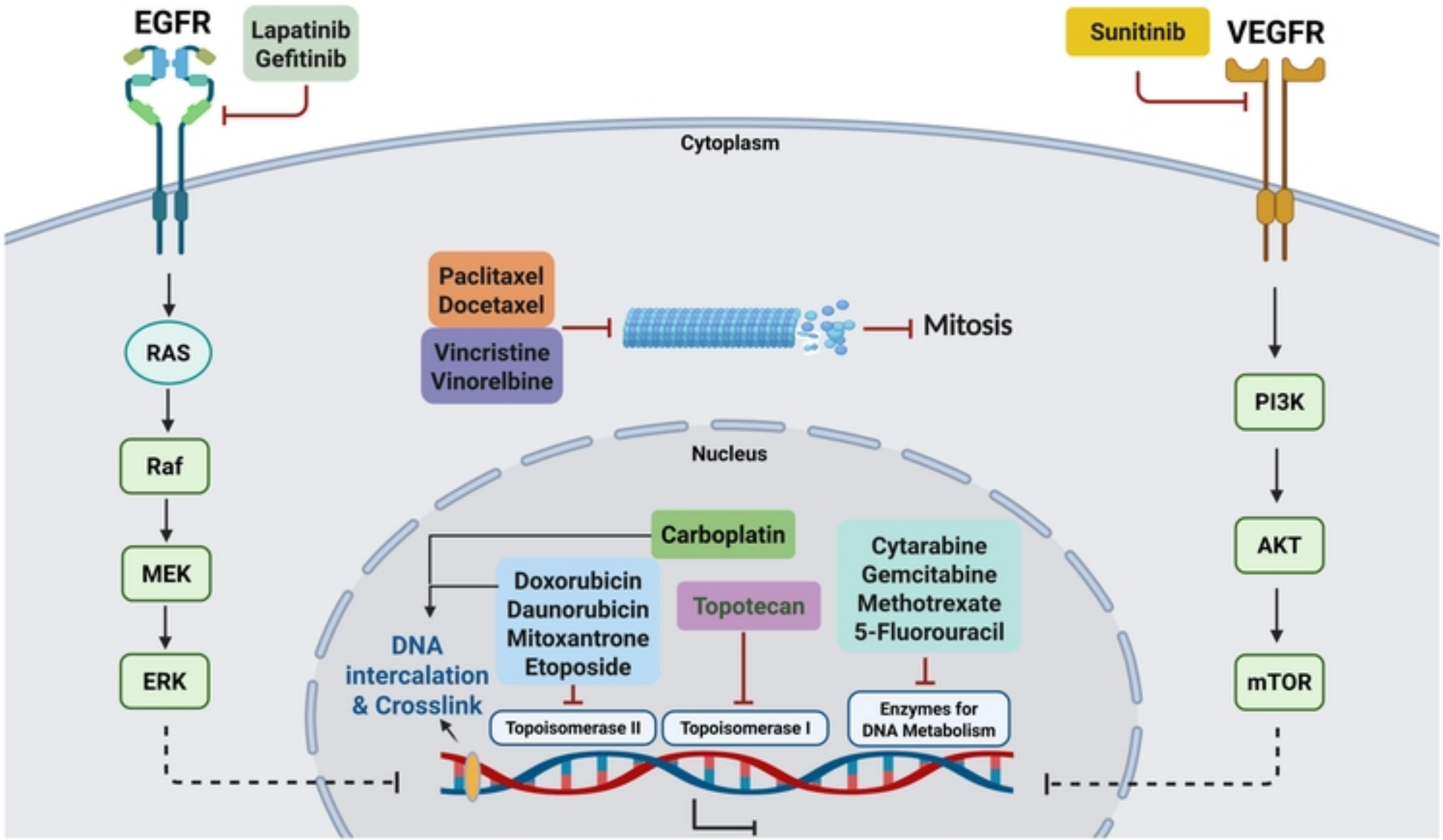
EGFR
Lapatinib
Gefitinib
Sunitinib
VEGFR
Cytoplasm
Paclitaxel
Docetaxel
Vincristine
Vinorelbine
Mitosis
RAS
Raf
MEK
ERK
PI3K
AKT
mTOR
Nucleus
Carboplatin
Doxorubicin
Daunorubicin
Mitoxantrone
Etoposide
Topotecan
Cytarabine
Gemcitabine
Methotrexate
5-Fluorouracil
DNA
intercalation
& Crosslink
Topoisomerase II
Topoisomerase I
Enzymes for
DNA Metabolism

Figure 11

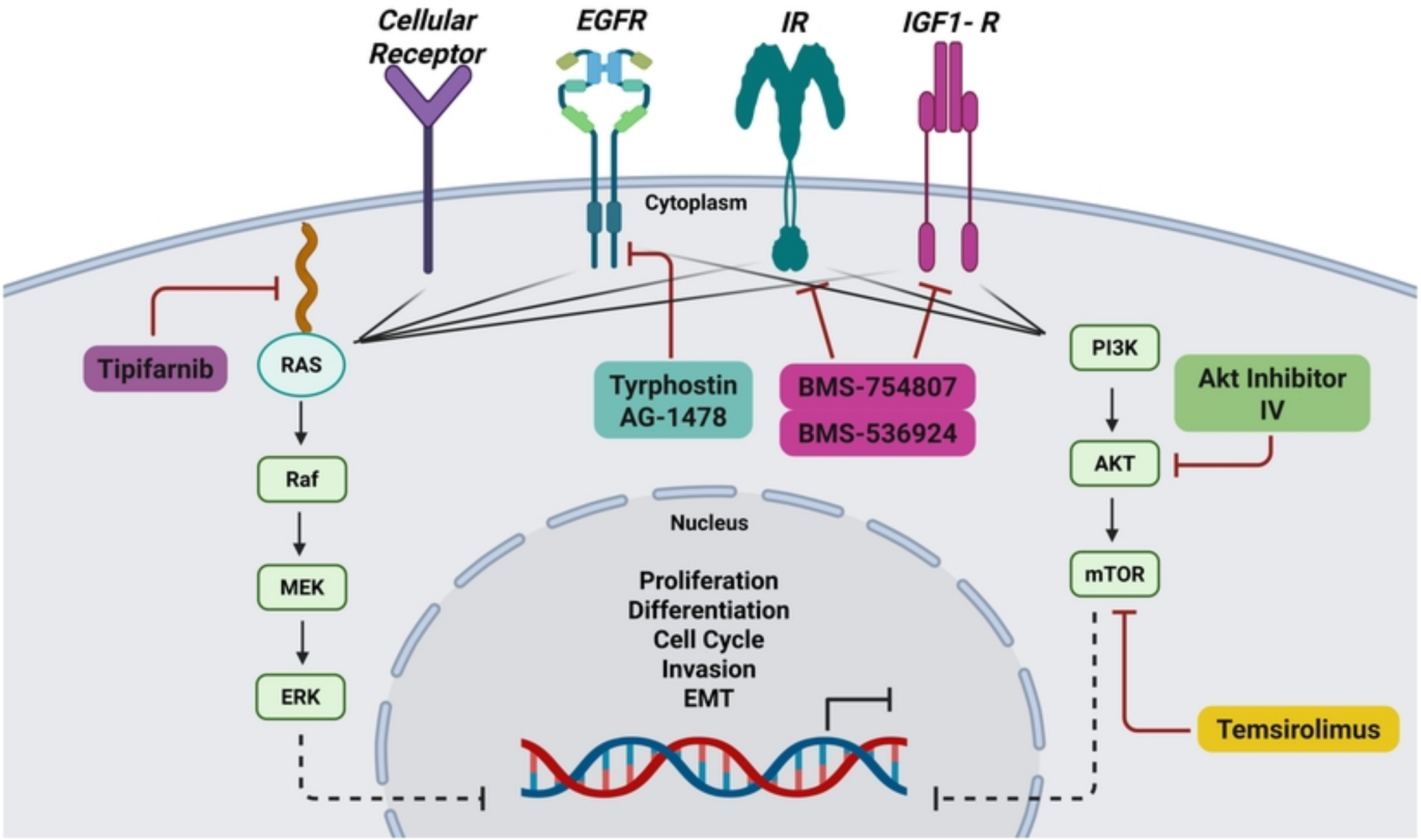
Cellular Receptor
EGFR
IR
IGF1- R
Cytoplasm
Tipifarnib
RAS
Raf
MEK
ERK
Tyrphostin AG-1478
BMS-754807
BMS-536924
PI3K
AKT
mTOR
Akt Inhibitor IV
Temsirolimus
Nucleus
Proliferation
Differentiation
Cell Cycle
Invasion
EMT

Figure 12